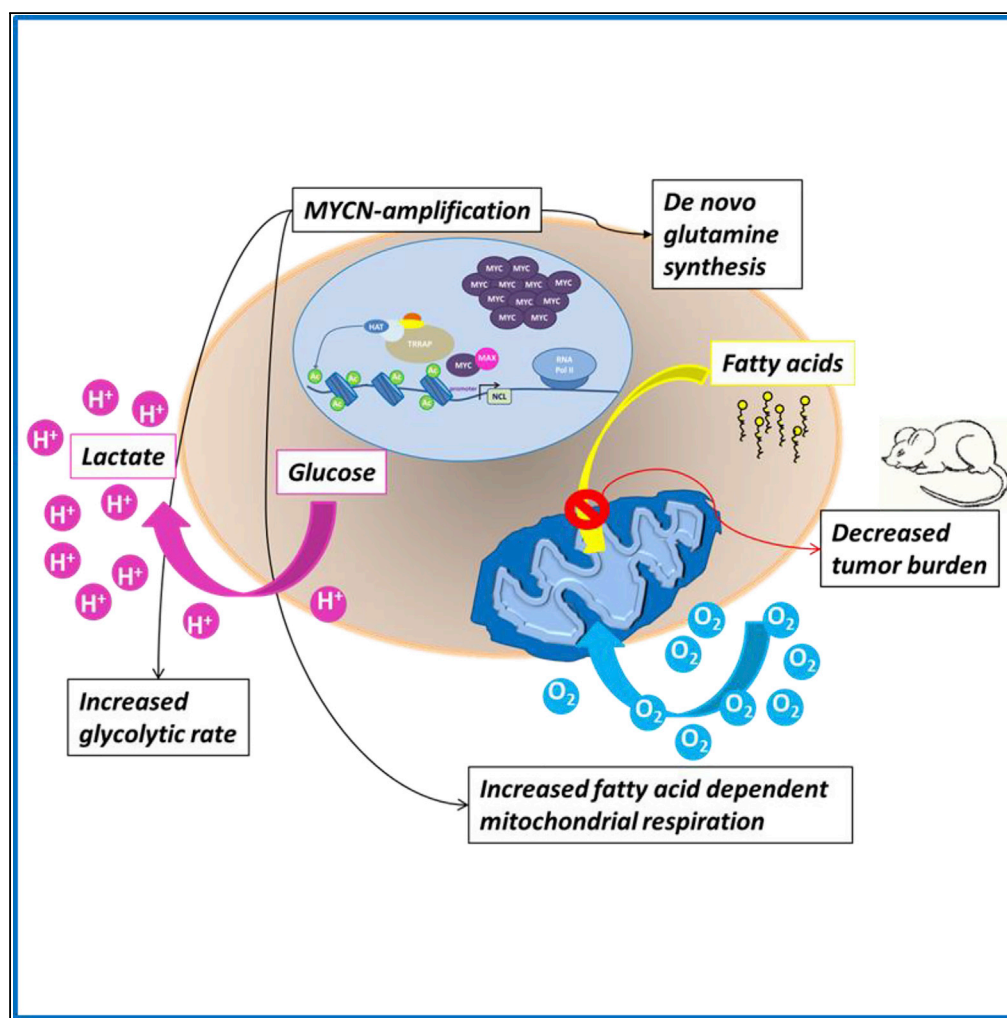


## Article

# MYCN-enhanced Oxidative and Glycolytic Metabolism Reveals Vulnerabilities for Targeting Neuroblastoma



Ganna Oliynyk,  
María Victoria  
Ruiz-Pérez,  
Lourdes Sainero-  
Alcolado, ...,  
Roland Nilsson,  
Janne Lehtiö,  
Marie Arsenian-  
Henriksson

marie.arsenian.henriksson@ki.se

## HIGHLIGHTS

High MYCN expression enhances glycolysis and oxidative phosphorylation in neuroblastoma

Neuroblastoma cells with MYCN-amplification display *de novo* glutamine synthesis

MYCN-amplified cells show fatty acid-dependent mitochondrial respiration

Fatty acid oxidation is a vulnerability in MYCN-amplified neuroblastoma

Oliynyk et al., iScience 21,  
188–204  
November 22, 2019 © 2019  
The Author(s).  
[https://doi.org/10.1016/  
j.isci.2019.10.020](https://doi.org/10.1016/j.isci.2019.10.020)

## Article

# MYCN-enhanced Oxidative and Glycolytic Metabolism Reveals Vulnerabilities for Targeting Neuroblastoma

Ganna Oliynyk,<sup>1,10</sup> María Victoria Ruiz-Pérez,<sup>1,10</sup> Lourdes Sainero-Alcolado,<sup>1</sup> Johanna Dzieran,<sup>1</sup> Hanna Zirath,<sup>1,2</sup> Héctor Gallart-Ayala,<sup>3,4</sup> Craig E. Wheelock,<sup>3</sup> Henrik J. Johansson,<sup>5,6</sup> Roland Nilsson,<sup>7,8,9</sup> Janne Lehtiö,<sup>5,6</sup> and Marie Arsenian-Henriksson<sup>1,11,\*</sup>

## SUMMARY

**In pediatric neuroblastoma, MYCN-amplification correlates to poor clinical outcome and new treatment options are needed for these patients. Identifying the metabolic adaptations crucial for tumor progression may be a promising strategy to discover novel therapeutic targets. Here, we have combined proteomics, gene expression profiling, functional analysis, and metabolic tracing to decipher the impact of MYCN on neuroblastoma cell metabolism. We found that high MYCN levels are correlated with altered expression of proteins involved in multiple metabolic processes, including enhanced glycolysis and increased oxidative phosphorylation. Unexpectedly, we discovered that MYCN-amplified cells showed *de novo* glutamine synthesis. Furthermore, inhibition of  $\beta$ -oxidation reduced the viability of MYCN-amplified cells *in vitro* and decreased tumor burden *in vivo*, while not affecting non-MYCN-amplified tumors. Our data provide information on metabolic processes in MYCN expressing tumors, which could be exploited for the development of novel targeted therapies.**

## INTRODUCTION

Neuroblastoma (NB) is a heterogeneous childhood tumor of the sympathetic nervous system, originating from embryonal neural crest cells (Brodeur, 2003; Cheung and Dyer, 2013). MYCN-oncogene amplification is a strong clinical marker of aggressive disease and poor outcome and is present in ~40% of high-risk cases (Maris, 2010; Peifer et al., 2015). Importantly, an overall elevated MYC signaling is also predictive of high-risk and stage of the disease, independently from MYCN-amplification (Fredlund et al., 2008).

The MYCN transcription factor belongs to the MYC family of oncoproteins (comprising MYCN, c-MYC, and MYCL), whose expression is deregulated in a vast number of human cancers. MYC overexpression is functionally linked to most aspects of tumorigenesis (Dang, 2012; Meyer and Penn, 2008) and is involved in the regulation of nucleotide biosynthesis, ribosome and mitochondrial biogenesis, and other metabolic processes (Miller et al., 2012). Furthermore, MYC-regulated proliferation is associated with enhanced activity of mitochondrial processes, and MYC inhibition decreases metabolic activity of cancer cells, leading to reduced proliferation. In addition, it has been shown that MYC overexpressing cells use both oxidative phosphorylation (OXPHOS) as well as glycolysis for energy production (Morrish et al., 2008).

Despite an increasing recognition of the importance of tumor metabolism for cancer aggressiveness and progression, still very few reports exist on the metabolic properties of MYCN-amplified tumors. We have previously shown that MYCN inhibition in MYCN-amplified neuroblastoma cells leads to accumulation of cytoplasmic lipid droplets, a phenomenon linked to mitochondrial dysfunction and inhibition of fatty acid oxidation (Zirath et al., 2013).

Here, we have characterized the consequences of central metabolic alterations in NB. To obtain a deeper understanding of the role of MYCN in regulating metabolic changes in NB cells, we downregulated MYCN followed by an integrated analysis combining quantitative mass spectrometry proteomics (Branca et al., 2014) with transcriptome analysis of patient datasets (Kocak et al., 2013). Metabolic properties of neuroblastoma cells were characterized by functional assays and metabolic tracing experiments. Our findings show that MYCN-amplified NB cells and tumors display prominent protein and gene expression alterations in metabolic genes compared with non-MYCN-amplified NB, indicative of overall activated mitochondrial

<sup>1</sup>Department of Microbiology, Tumor and Cell Biology (MTC), Biomedicum B7, Karolinska Institutet, 171 65 Stockholm, Sweden

<sup>2</sup>The Dental and Pharmacological Benefits Agency, 104 22 Stockholm, Sweden

<sup>3</sup>Department of Medical Biochemistry and Biophysics (MBB), Karolinska Institutet, 171 65 Stockholm, Sweden

<sup>4</sup>Metabolomics Unit, University of Lausanne – UNIL, Lausanne, Switzerland

<sup>5</sup>Department of Oncology-Pathology, Karolinska Institutet, 171 21 Solna, Sweden

<sup>6</sup>Science for Life Laboratory, Cancer Proteomics Mass Spectrometry, 171 65 Stockholm, Sweden

<sup>7</sup>Center for Molecular Medicine, Karolinska Institutet, 171 76 Stockholm, Sweden

<sup>8</sup>Cardiovascular Medicine Unit, Department of Medicine, Karolinska Institutet, 171 76 Stockholm, Sweden

<sup>9</sup>Division of Cardiovascular Medicine, Karolinska University Hospital, 171 76 Stockholm, Sweden

<sup>10</sup>These authors contributed equally

<sup>11</sup>Lead Contact

\*Correspondence: marie.arsenian.henriksson@ki.se

<https://doi.org/10.1016/j.isci.2019.10.020>



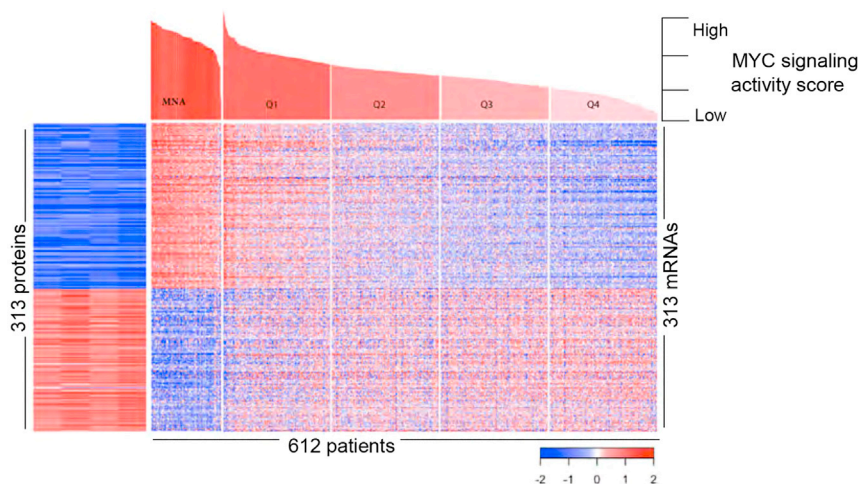


**Figure 1. Protein and mRNA Overlap of Metabolism-Related Genes Display Dependence on MYC Signaling Level**  
Heatmap displaying proteins involved in metabolic processes (left) and mRNA levels of the corresponding genes in NB patients (right). Red: upregulation; blue: downregulation. MYC signaling was inferred using gene expression (Fredlund et al., 2008). Top: the MYCN-amplified (MNA) cases were separated and the remaining samples were then subdivided into quartiles of inferred MYC signaling (Q1-4). The heatmap to the left shows changes in protein expression upon MYCN downregulation in BE(2)sh MYCN cells for 24 and 48 h, and the right heatmap shows the expression of the corresponding genes in 612 neuroblastoma patients (Kocak et al., 2013) divided according to MYC signaling or MNA cases as indicated. See also Figure S1.

and glycolytic function and unexpectedly associated with glutamine synthesis. Furthermore, we found that  $\beta$ -oxidation of fatty acids is a major contributor to mitochondrial oxidative processes.

Collectively, we have identified a promising approach to target MYCN-amplified tumors by demonstrating that inhibition of fatty acid oxidation led to a reduced tumor burden in MYCN-amplified xenograft models, whereas not affecting non-MYCN-amplified tumors.

## RESULTS

### Overlap of the Protein and mRNA Profiles of MYCN-amplified NB Cells and Tumors Shows Dependency on the Level of MYC Signaling

To identify differentially regulated metabolic pathways in MYCN-amplified versus non-MYCN-amplified tumor samples and establish the connection to a cell line model with adjustable MYCN levels, we combined information from protein levels *in vitro* with mRNA expression from patient datasets (Kocak et al., 2013). In order to explore how MYCN accounts for relevant metabolic processes, we performed high-resolution mass spectrometry quantitative proteomics following MYCN downregulation (Figure S1A) (Branca et al., 2014; Kall et al., 2007) in MYCN-amplified SK-N-BE(2) cells stably expressing a small hairpin construct against MYCN under the control of an inducible doxycycline promoter, BE(2)sh MYCN (Henriksen et al., 2011). MYCN levels were either high due to the MYCN-amplification in untreated cells, termed "BE(2)sh MYCN ON" or downregulated upon treatment with doxycycline in "BE(2)sh MYCN OFF" cells (Figure S1B). In total, 6504 proteins were identified and 4779 passed initial quality controls (Figure S1C). Out of these, 1781 (37%) were significantly differentially up- or downregulated at a cutoff 1.4 and 0.7, respectively, in the same direction at both 24 and 48 h when comparing doxycycline-treated with nontreated BE(2)sh MYCN cells (Table S1). The proteomics findings were validated using immunoblotting (Figure S1D).

Gene Set Enrichment Analysis (GSEA) identified metabolism as one of the most affected processes in NB cells. We asked if these differences in protein levels *in vitro* relate to gene expression differences in NB patients (Figure 1). To this end, we compared metabolic proteins affected by MYCN regulation with mRNA expression data from neuroblastoma primary tumors (Kocak et al., 2013). The proteomics data show up- (in red) and downregulated (in blue) proteins upon MYCN downregulation. Notably, we observed that the protein expression pattern after MYCN downregulation *in vitro* was opposite to the mRNA expression

levels of the corresponding genes in patients with MYCN-amplification, whereas it showed a similar pattern to that of patients with lower MYC signaling (Figure 1 and Table S2). This highlights the adequacy of our *in vitro* model system to study the impact of MYCN on metabolic processes while reflecting MYCN-associated expression patterns in patients. These data suggest that MYCN-amplification alters key metabolic pathways as glycolysis and gluconeogenesis, fatty acid biosynthesis, citric acid cycle, mitochondrial electron transport chain, glutathione metabolism, and redox enzymes (Figures S2–S4).

### MYCN Levels Are Linked to Metabolic Programs and Clinical Outcome

Analysis of gene and protein expression in BE(2)*sh* MYCN ON versus BE(2)*sh* MYCN OFF cells revealed prominent differences in the main metabolic pathways. Combined mapping of mRNA and protein expression shows altered levels of several glycolytic enzymes (Figure S2), including hexokinase isoform 2 (HK2), which has been previously implicated in NB (Klepinin et al., 2014). We next analyzed overall survival in two neuroblastoma patient cohorts with similar proportions of MYCN-status and patient data covering all five INSS stages (Figure S1E; Kocak et al., 2013; Molenaar et al., 2012). High levels of HK2 were correlated with poor clinical outcome (Figures 2A and S1F) and we also observed that HK2 expression was related to MYCN levels in NB tumors and cells (Figures 2B and 2C).

In addition, enzymes of the tricarboxylic acid cycle (TCA) and the electron transport chain (ETC) were also overexpressed in MYCN-amplified cells and tumors (Figures S2 and S3). The enzymes citrate synthase (CS), isocitrate dehydrogenase isoform 2 (IDH2), and alpha ketoglutarate dehydrogenase-like (OGDHL) were found to have enhanced expression both at the mRNA and at the protein levels in MYCN-amplified cells and patients (Figure S2). High mRNA expression of the genes encoding the majority of TCA enzymes significantly correlated to poor patient survival (Figure S2). Importantly, we also demonstrated major alterations at the protein and mRNA levels of complexes of the ETC and in the ATP synthase (Figure S3). Most of these respiratory subunits were upregulated in MYCN-amplified cells and tumors, although some subunits were also found to be downregulated. Notably, high expression of the MYCN-associated respiratory subunit genes correlated to poor overall survival (Figure S3).

Gene and protein expression data showed an enhanced expression of key antioxidant-mediating enzymes in MYCN-amplified cells and tumors (Figure S4). Among them were several enzymes of glutathione metabolism (Figures S4A and S4B) and of glutathione-linked ROS detoxification (Figure S4C). Furthermore, members of the peroxiredoxin ROS scavenger system, including peroxiredoxin 6 (PRDX6), were upregulated in MYCN-amplified tumors and/or cells (Figure S4C). High mRNA expression levels of the majority of the MYCN-associated antioxidant regulating enzymes (Figure S4C) correlated to worse prognosis and a reduced overall survival in NB patients. We investigated the impact of MYCN expression on OXPHOS in NB cells in more detail. Gene set enrichment analysis (GSEA) of the protein profile of BE(2)*sh* MYCN cells demonstrated that proteins positively regulated by MYCN were associated with aerobic respiration and mitochondrial translation processes (Figure 2D). Data analysis suggested that the majority of mitochondrial proteins are overexpressed in MYCN-amplified NB cells and tumors (Figure S2 and Table S1). The gene encoding the transcription factor nuclear respiratory factor 1 (NRF1), which regulates mitochondrial biogenesis through activation of key metabolic enzymes essential for mitochondrial translation and respiration (Huo and Scarpulla, 2001), was found upregulated in MYCN-amplified cells and correlated to reduced survival probability in neuroblastoma patients (Figure 2E and Table S1). We used transmission electron microscopy (TEM) to show intact mitochondrial architecture in BE(2)*sh* MYCN ON and Tet-21/N ON cells, whereas reduced electron density and an increased number of damaged *cristae* were found in the mitochondria of BE(2)*sh* MYCN OFF and of Tet-21/N OFF cells (Figures 2F and S1I). Notably, MYCN down-regulation was associated with decreased number as well as swelling of mitochondria (Figures 2F and S1I). Members of both the mitochondrial fission as well as fusion machinery were upregulated in MYCN-amplified tumors and/or cells (Tables S1 and S2), including optic atrophy 1 (OPA1) and mitochondrial fission process 1 (MTFP1). In addition, high mRNA expression levels of OPA1 and MTFP1 correlated with worse prognosis and reduced overall survival in NB patients (Figures 2G and S1J).

Although the analysis of whether the regulation of metabolic genes occurred by direct or indirect transcriptional activity of MYCN is out of the scope of the present study, we compared the 313 metabolic proteins from our proteomics analysis shown in Figure 1 with a list of direct MYCN targets in neuroblastoma cell lines previously published (Hsu et al., 2016). These authors used chromatin-immunoprecipitation (ChIP)-sequencing to identify direct MYCN target genes. We found that 45 of our proteins were present in their list of MYCN targets and importantly, that the direction of the *sh*MYCN regulation of these proteins

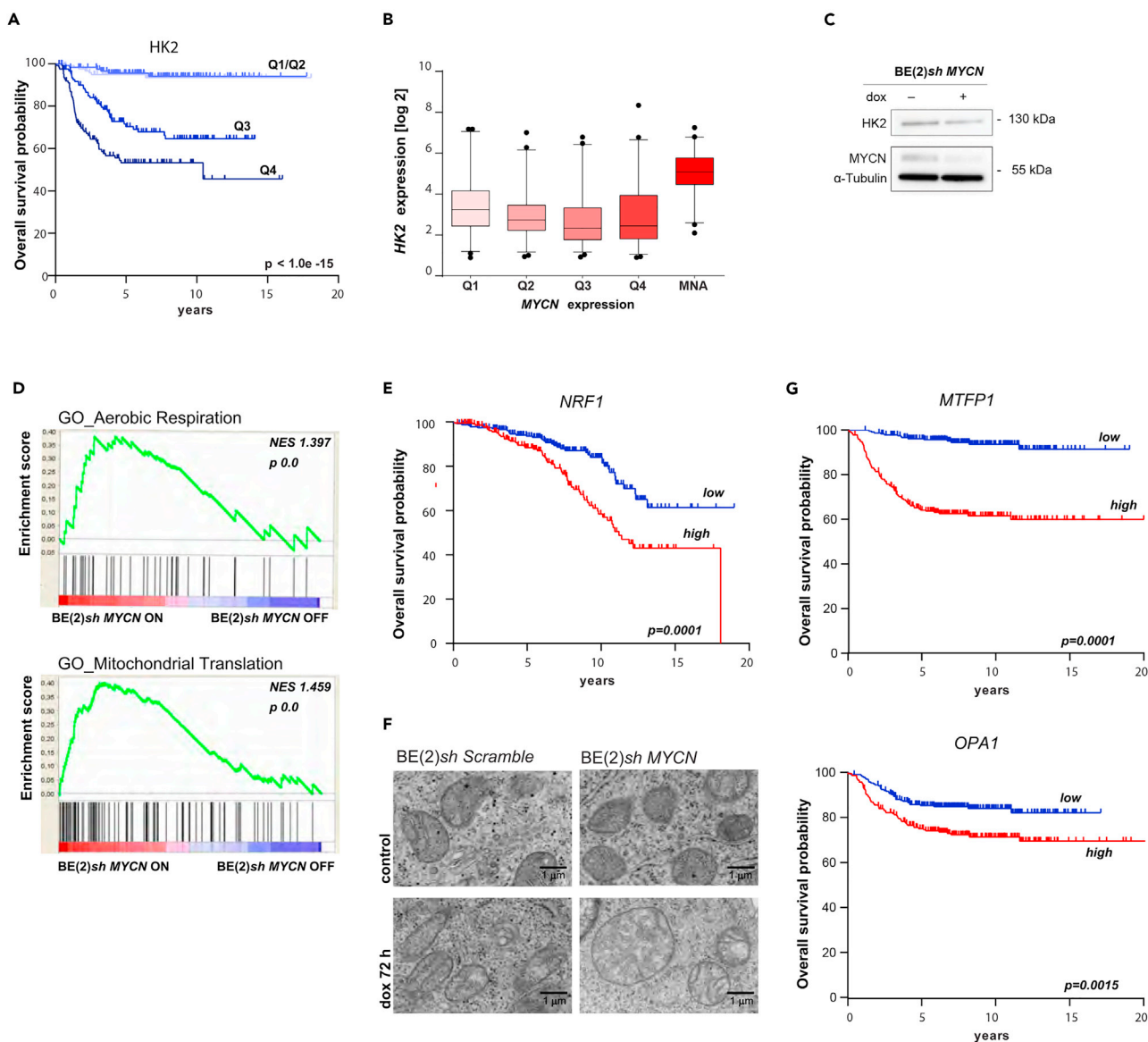


**Figure 2. MYCN Levels Are Linked to Metabolic Programs and Clinical Outcome**

(A) Kaplan-Meier plot showing overall survival of NB patients based on *HK2* mRNA levels subdivided into expression quartiles (Q1-4).  
 (B) Boxplots of *HK2* expression based on quartiles of MYC signaling and MYCN-amplified cases in clinical NB samples (Kocak et al., 2013; Fredlund et al., 2008).  
 (C) Immunoblot showing *HK2* protein expression after treatment of BE(2)sh MYCN cells with 2  $\mu$ g/mL doxycycline as indicated. Representative blot from three independent experiments is shown;  $\alpha$ -tubulin was used as a loading control.  
 (D) Gene Ontology (GO) aerobic respiration and mitochondrial translation enrichment plots (using c5.bp.v5.2.symbols.gmt gene set derived from the Biological Process Ontology) in BE(2)sh MYCN ON vs. BE(2)sh MYCN OFF NB cells. Red: upregulation; blue: downregulation.  
 (E) Kaplan-Meier overall survival curve from the Kocak cohort based on the mRNA expression of the *NRF1* gene.  
 (F) Transmission electron microscopy images of representative mitochondria in BE(2)sh Scramble and BE(2)sh MYCN cells. Cells were treated with vehicle or 2  $\mu$ g/mL doxycycline for 72 h. Scale bars indicate 1  $\mu$ m.  
 (G) Kaplan-Meier overall survival curves from the Kocak cohort based on the mRNA expression of the *MTFP1* and *OPA1* genes.  
 See also Figures S2–S4.

was in all cases contrary to the action of MYCN (activation/repression) these authors describe for the corresponding genes. Thus, if MYCN activates a particular gene, we observed that shMYCN downregulated the corresponding protein and *vice versa* for all of these 45 proteins (Table S3). MYCN could indirectly modify the levels of the other proteins shown in Figure 1 through the plethora of transcriptional regulators

controlled by this oncoprotein (Hsu et al., 2016) or by other regulatory loops. Furthermore, additional proteins affected by shMYCN could be direct MYCN-targets not identified by Hsu et al. (2016). In summary, our data analysis suggests that MYCN increases expression of glycolytic and mitochondrial enzymes and highlights the importance of metabolism in mediating tumor aggressiveness in MYCN-amplified NB.

### MYCN Increases the Glycolytic and OXPHOS Capacity of MYCN-amplified NB Cells

To investigate the functional impact of MYCN on metabolism in NB cells we employed extracellular flux-based analyses. We compared the glycolytic capacity of three cell lines in which MYCN expression can be regulated with doxycycline, BE(2)sh MYCN, Kelly shMYCN, and Tet-21/N (Figures S1B and S1H), before and after MYCN downregulation, as well as of non-MYCN-amplified NB cells. Glycolytic parameters (basal glycolysis, glycolysis, glycolytic capacity, and glycolytic reserve) were assessed by measuring the extracellular acidification rate (ECAR) (Figure S5A). We found that all parameters were significantly reduced after 72 h of MYCN inhibition in two different MYCN-amplified NB cell lines and in the Tet-21/N MYCN-overexpressing NB cell line (Figures 3A and 3B). Examination of the ECAR in the non-MYCN-amplified SH-EP, SK-N-SH, and SK-N-AS NB cell lines revealed reduced ECAR for all glycolytic parameters in comparison with BE(2)sh MYCN cells (Figure 3A). Taken together, our results demonstrate that MYCN-amplification is associated with enhanced glycolytic activity in NB.

Next, we analyzed key parameters of respiration in several MYCN-amplified and non-MYCN-amplified NB cells by measuring the oxygen consumption rate (OCR) (Figure S5B): basal, ATP-coupled, maximal/uncoupled respiration, as well as the spare/reserve respiration. Our analysis showed that MYCN-amplified NB cells and MYCN-overexpressing Tet-21/N cells displayed increased OCR levels compared with non-MYCN-amplified NB and cells with MYCN downregulation (Figures 3C and 3D). Both basal and maximal respiration were significantly higher in BE(2)sh MYCN ON cells compared with cells after 72 h of MYCN downregulation (BE(2)sh MYCN OFF) or non-MYCN-amplified NB cells (Figures 3C and 3D). In addition, ATP-coupled and increased uncoupled respiration indicated that MYCN expression promotes energy production via oxidative phosphorylation. Together, gene expression and functional assays demonstrate that MYCN positively regulates mitochondrial respiration in MYCN-amplified NB cells.

To evaluate the ability of the cells to regulate both glycolytic flux and mitochondrial respiration as a response to induced metabolic stress, we used the ATP synthase inhibitor oligomycin and the mitochondrial uncoupler FCCP, respectively (Figure 3E). Inhibition of ATP synthase forced all cell lines to increase the glycolysis rate to compensate for the lack of mitochondrial energy production to a similar extent, independently of their MYCN status (Figure 3F). Uncoupling of ETC by FCCP increased mitochondrial respiration to maximum levels. Although all cells increased OXPHOS upon uncoupling, the elevation was significantly higher in BE(2)sh MYCN ON cells in comparison to MYCN OFF, SH-EP, and SK-N-SH cells (Figure 3F). In conclusion, we found that the stressed phenotype of the BE(2)sh MYCN ON cells was characterized by a shift in the metabolic balance toward robustly increased oxidative phosphorylation as well as enhanced aerobic glycolysis. In contrast, BE(2)sh MYCN OFF, SH-EP, and SK-N-SH cells increased glycolysis in a similar range but were not able to generate such a strong OXPHOS stress response.

### Contribution of Glucose, Glutamine, and Fatty Acids to OXPHOS

The obtained results indicated that MYCN-amplified NB cells are characterized by both enhanced glycolysis and mitochondrial respiration. We next analyzed the contribution of the three crucial mitochondrial fuels—glucose, glutamine, and fatty acids. We measured OCR in the presence or absence of specific inhibitors of the corresponding oxidation pathways. We used UK5099, an inhibitor of the mitochondrial pyruvate transporter (MPT), to evaluate the impact of glucose on respiration, whereas the fatty acid oxidation pathway was inhibited by etomoxir, which inhibits carnitine palmitoyltransferase 1 (CPT1C), the rate-limiting enzyme of  $\beta$ -oxidation. To determinate glutamine oxidation we employed the kidney-type glutaminase 1 (GLS1) inhibitor BPTES. The decreased respiration in response to inhibition of the oxidation pathways determinates the capacity of the cells to oxidize a particular fuel. We found that approximately 65% of the mitochondrial respiratory capacity in MYCN-amplified NB cells was dependent on fatty acid oxidation (FAO) (Figures 4A, 4B, S5C, and S5D). Surprisingly, our results demonstrated glutamine independence of mitochondrial respiration in MYCN-amplified NB cells compared with non-MYCN-amplified NB and MYCN OFF cells (Figures 4A and 4B). Thus, our data suggest that fatty acids are an important fuel for mitochondrial respiration in NB cells. Indeed, mitochondrial oxidation of glutamine was significantly lower than oxidation of fatty acids and/or glucose in MYCN-amplified NB cells. Furthermore, the ability to oxidize

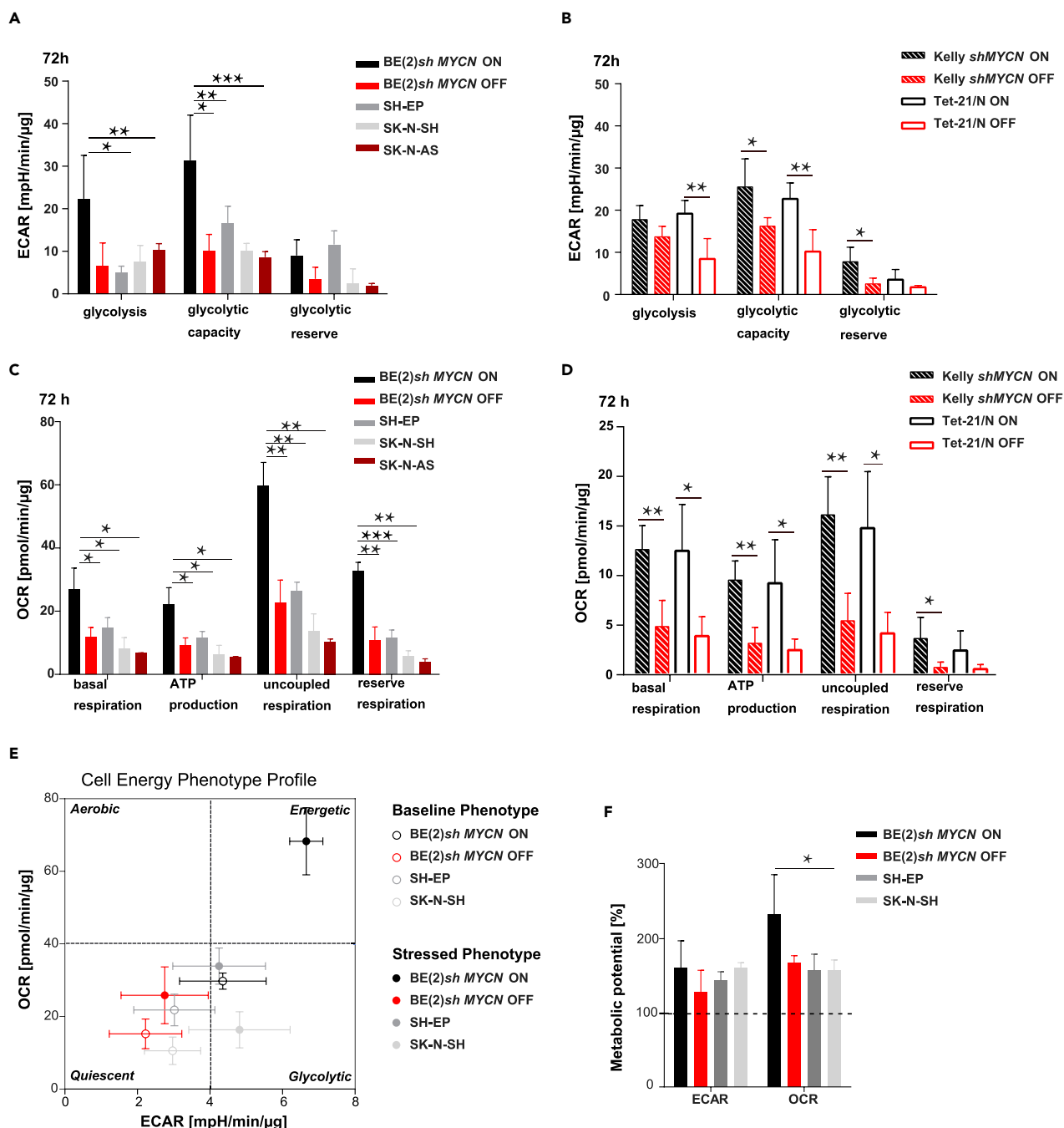


**Figure 3. MYCN Increases the Glycolytic and OXPHOS Capacity of MYCN-amplified NB Cells**

(A) Quantification of extracellular acidification rate (ECAR) in BE(2)sh MYCN ON, BE(2)sh MYCN OFF, SK-N-SH, SH-EP, and SK-N-AS cells. (B) Quantification of ECAR levels in Kelly shMYCN and Tet-21/N cells before and after regulation of MYCN expression as indicated. (C) Quantification of oxygen consumption rate (OCR) in BE(2)sh MYCN ON, BE(2)sh MYCN OFF, SK-N-SH, SH-EP, and SK-N-AS cells. (D) Quantification of OCR levels in Kelly shMYCN and Tet-21/N cells before and after regulation of MYCN expression as indicated. (E) Baseline and stressed phenotype (open and filled circles, respectively) of BE(2)sh MYCN before and after downregulation of MYCN expression, SK-N-SH, and SH-EP cells, as indicated. (F) Visualization of the increase of metabolic potential in the experiments shown in (E). All data are presented as the mean  $\pm$  SD of three independent experiments performed at 72 h of MYCN regulation, with \*, \*\*, \*\*\* indicating  $p < 0.05$ ,  $p < 0.01$  and  $p < 0.001$ , respectively. See also Figure S5.

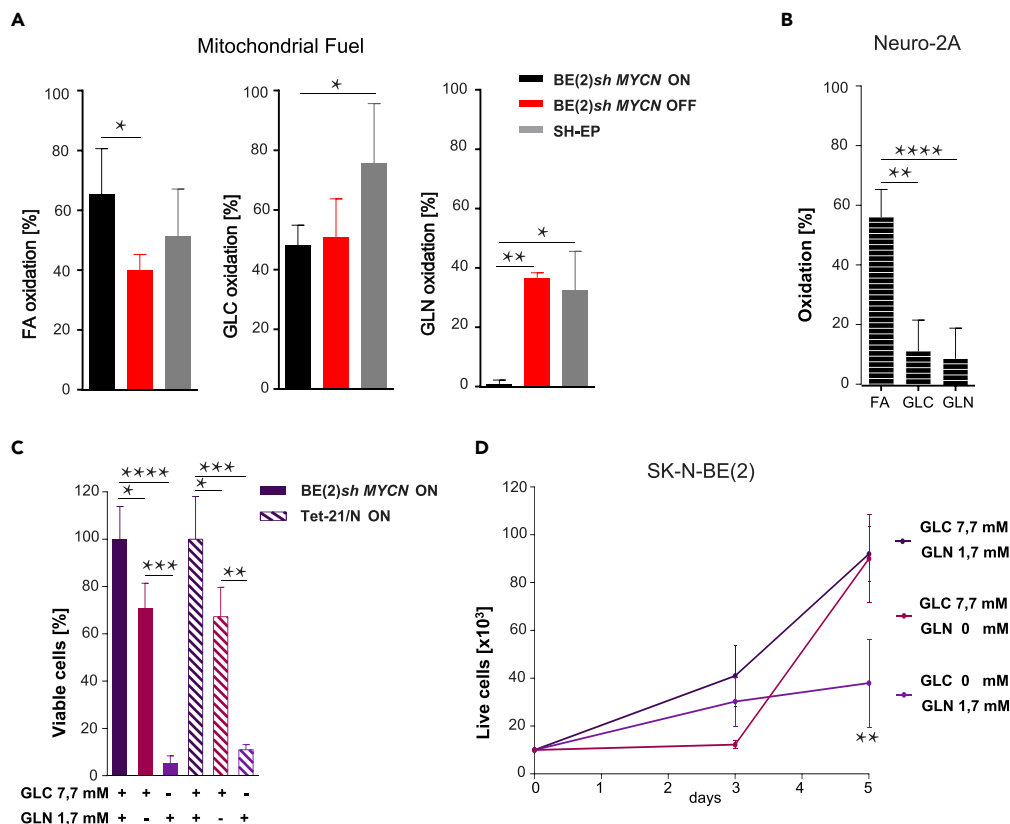


**Figure 4. Relative Contribution of Glucose, Glutamine, and Fatty Acids to OXPHOS**

(A) Quantification of OCR in BE(2)sh MYCN cells before and after downregulation of MYCN for 72 h and in SH-EP cells as indicated. FA = fatty acids, GLC = glucose, GLN = glutamine.

(B) Quantification of OCR in Neuro-2A mouse neuroblastoma cells.

(C) WST-1 assay showing percentage of viable BE(2)sh MYCN ON and Tet-21/N ON cells after five days in substrate-restricted medium as indicated.

(D) Number of viable SK-N-BE(2) cells during five days in substrate-limited conditions determined by cell counting at the indicated time points.

All data are presented as mean  $\pm$  SD from three independent experiments, with \*, \*\*, \*\*\*, \*\*\*\* indicating  $p < 0.05$ ,  $p < 0.01$ ,  $p < 0.001$  and  $p < 0.0001$ , respectively.

See also Figure S5.

glutamine was increased in BE(2)sh MYCN OFF cells compared with BE(2)sh MYCN ON cells. In addition, oxidation of glutamine was also higher in SH-EP non-MYCN-amplified cells than in BE(2)sh MYCN ON cells or in Neuro-2A mouse neuroblastoma cells, and similar to the BE(2)sh MYCN OFF cells (Figures 4A and 4B). Since glutamine is a substrate commonly oxidized in cultured cells, the low glutamine oxidation in BE(2)sh MYCN ON NB cells was unexpected. To evaluate the impact of glucose and glutamine on cell survival we determined the viability of MYCN-amplified NB cells upon starvation conditions. Five days of glucose deprivation resulted in 90% reduction of viable BE(2)sh MYCN ON, SK-N-BE(2), and Tet-21/N cells. In contrast, glutamine withdrawal alone reduced cell viability only by 30% compared with complete medium conditions, and MYCN-amplified NB cells demonstrated glutamine independent proliferation after an initial adaptation time (Figures 4C and 4D). Taken together, our results highlight a low glutamine oxidation rate and only a small impact of glutamine starvation in highly proliferative MYCN-amplified NB cells.

### Neuroblastoma Cells Are Able to Synthesize Glutamine

As mentioned above, when we compared the ability of NB cells to oxidize glucose, glutamine and fatty acids, we found that MYCN-amplified NB cells display reduced glutamine oxidation and the ability to survive glutamine starvation. To further investigate this phenotype, we performed isotope tracing experiments with U- $^{13}\text{C}_6$ -glucose and U- $^{13}\text{C}_5$ -glutamine, respectively. In BE(2)sh MYCN ON cells, glucose was

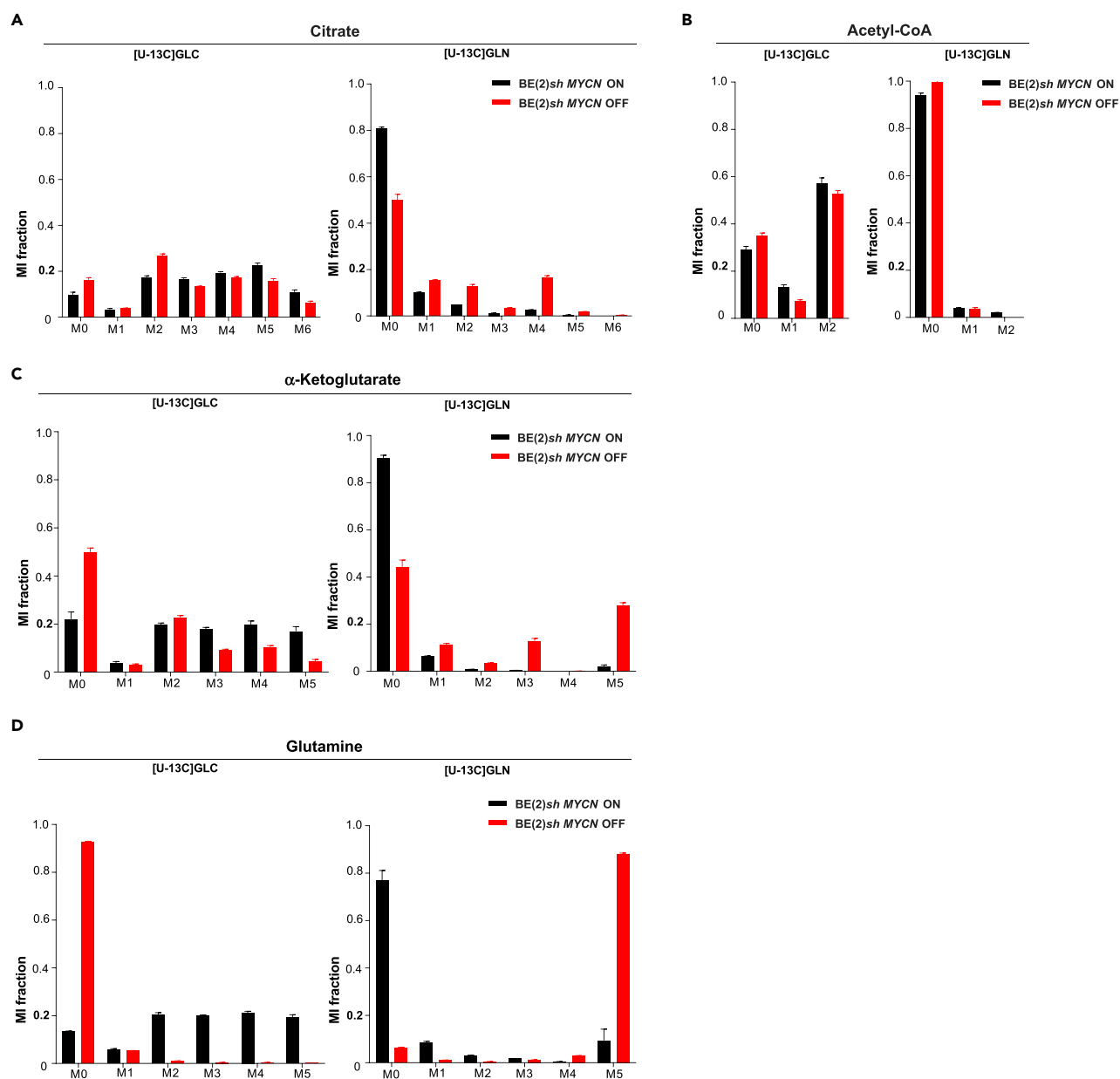


### Figure 5. MYCN-amplified NB Cells Exhibit *De Novo* Glutamine Synthesis Pattern

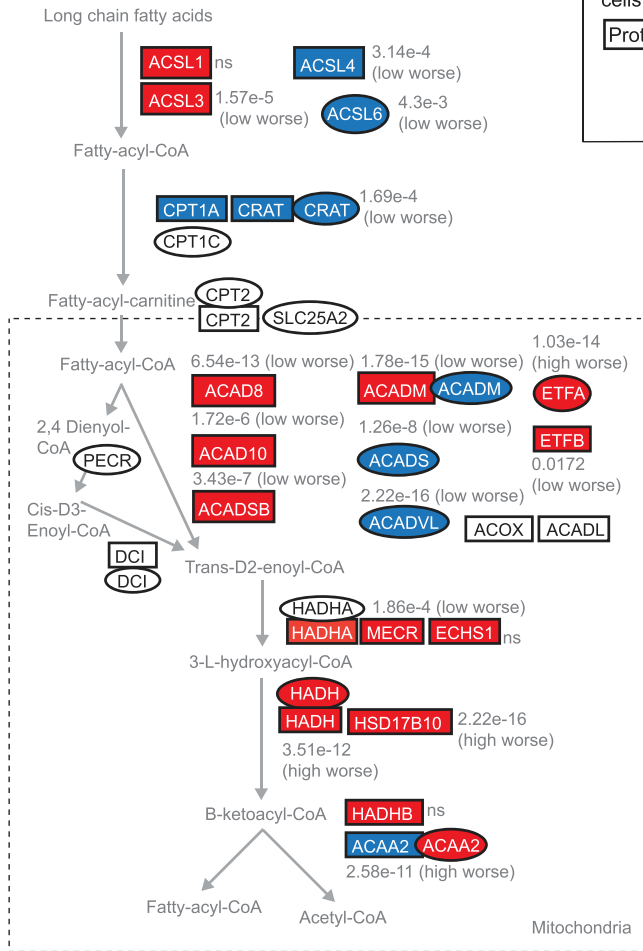
(A–D) The contribution of glucose and glutamine toward TCA-cycle metabolites was measured by metabolic tracing using U- $^{13}\text{C}_6$ -glucose or U- $^{13}\text{C}_5$ -glutamine in BE(2)sh MYCN cells as indicated. Comparison of mass isotopologue distributions (MID) of citrate (A), acetyl-CoA (B),  $\alpha$ -ketoglutarate (C), and glutamine (D) in BE(2)sh MYCN ON and in BE(2)sh MYCN OFF cells after five days of MYCN downregulation with 2  $\mu\text{g}/\text{mL}$  doxycycline. MI of labeled carbons as indicated (M0–M6).

See also [Figure S6](#).

a major source of TCA cycle carbon, because U- $^{13}\text{C}_6$ -glucose cultures exhibited 55%  $^{13}\text{C}$  enrichment of citrate, with a prominent  $^{13}\text{C}_2$  mass isotopomer (Figure 5A), and 64% of acetyl-CoA, mainly as  $^{13}\text{C}_2$  (Figure 5B), whereas U- $^{13}\text{C}_5$ -glutamine gave only 4%  $^{13}\text{C}$  enrichment in  $\alpha$ -ketoglutarate, mostly as  $^{13}\text{C}_5$  (Figure 5C). After MYCN inhibition, the glucose contribution to citrate and acetyl-CoA diminished somewhat (Figures 5A and 5B), whereas glutamine contribution to  $\alpha$ -ketoglutarate and citrate increased markedly (Figures 5A–5C), suggesting a switch toward oxidation of glutamine, presumably by activation of glutaminase. In addition, the contribution of glucose to other intermediates of the Krebs cycle decreased in

A

Fatty acid oxidation

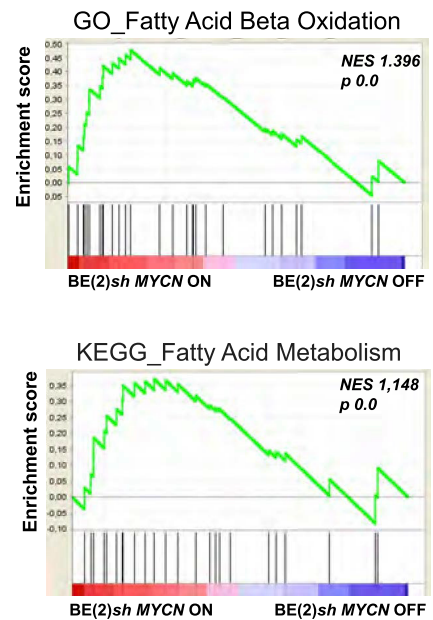


Differential levels of proteins in BE(2)sh MYCN ON cells and mRNAs in patient cohort

Protein mRNA

- Upregulated
- Downregulated
- Unchanged

B



C

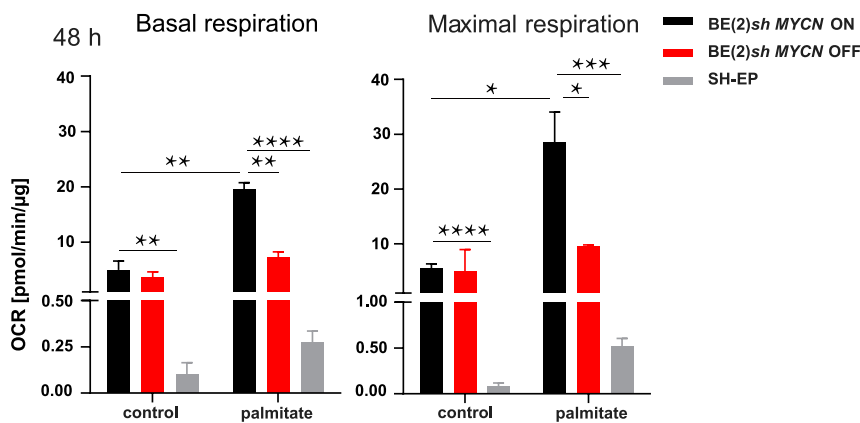


### Figure 6. Fatty Acid $\beta$ -oxidation in MYCN-amplified NB Cells

(A) Schematic picture showing significantly regulated mRNAs and proteins involved in  $\beta$ -oxidation of fatty acids, based on KEGG pathway maps. Red and blue colors represent up- and downregulated mRNAs (ovals) in MYCN-amplified versus non-MYCN amplified tumors, or proteins (rectangles) in BE(2)sh MYCN ON versus BE(2) sh MYCN OFF cells. The correlation of expression of different genes (high or low) to patient survival using the Oberthuer patient dataset (Oberthuer et al., 2006) is indicated. ns= not statistically significant.

(B) Gene ontology fatty acid  $\beta$ -oxidation enrichment plot (using c5.bp.v5.2.symbols.gmt gene set derived from the Biological Process Ontology) in BE(2)sh MYCN ON versus BE(2)sh MYCN OFF cells.

(C) Left graph shows quantification of basal OCR in BE(2)sh MYCN and SH-EP cells. Right graph shows quantification of maximal OCR (in response to 2  $\mu$ M FCCP) in the same cells.

All data are presented as the mean  $\pm$  SD of three independent experiments, with \*, \*\*, \*\*\*, \*\*\*\* indicating  $p < 0.05$ ,  $p < 0.01$ ,  $p < 0.001$  and  $p < 0.0001$ , respectively.

MYCN OFF cells as well (Figures S6A and S6B). In both conditions, about one-third of TCA cycle carbons were derived from an unknown ( $^{12}$ C) source, potentially fatty acids.

We noted that most of the intracellular glutamine was not labeled from U- $^{13}$ C<sub>5</sub>-glutamine in BE(2)sh MYCN ON cells, suggesting that it was not derived from uptake from the medium. Instead, we found that a majority of the cellular glutamine was synthesized from glucose via  $\alpha$ -ketoglutarate (Figures 5C and 5D). At this time point, the medium glutamine concentration was  $\sim$ 1 mM, showing that this phenomenon was not due to the exhaustion of glutamine. In contrast, in BE(2)sh MYCN OFF cells, there was almost no glutamine synthesis, and instead most of the glutamine was derived from the medium (Figure 5D). Such glutamine synthesis pattern is uncommon in cancer cells. To support our findings, we performed tracing experiments with both U- $^{13}$ C<sub>5</sub>-glucose and U- $^{13}$ C<sub>5</sub>-glutamine in two different MYCN-amplified or overexpressing cell lines where we inhibited MYCN using the small chemical MYC/MYCN-inhibitor 10058-F4 (Muller et al., 2014) or by doxycycline. In SK-N-BE(2) cells, we obtained  $\sim$ 60%  $^{13}$ C<sub>5</sub> glutamine, indicating that the major part of glutamine carbons was derived from medium glutamine, but we also observed  $^{13}$ C<sub>2</sub>,  $^{13}$ C<sub>3</sub>, and  $^{13}$ C<sub>4</sub> mass isotopomers (Figure S6C), suggesting glutamine synthesis from glucose. In Tet-21/N cells, most glutamine appeared to be synthesized from glucose (Figure S6D), similar to BE(2)sh MYCN cells. In both cell lines, MYCN inhibition prevented *de novo* synthesis of glutamine. The lack of glutamine synthesis in MYCN OFF cells was likely mediated by inhibition of glutamate-ammonia ligase, because glutamate remained labeled from U- $^{13}$ C<sub>6</sub>-glucose in BE(2)sh MYCN OFF cells (Figure S6E). In neither condition was glutamine converted to lactate ("glutaminolysis") (Figure S6F).

### Fatty Acid $\beta$ -oxidation in MYCN-amplified NB Cells

The above results show that fatty acids greatly contribute to OXPHOS in MYCN-amplified cells (Figures 4A, 4B, S5C, and S5D), and a more detailed analysis of gene and protein data confirmed that MYCN-amplification was indeed linked to the expression of enzymes involved in FAO (Figures 6A and 6B). Specifically, we found that high expression of the genes encoding the enzymes involved in regulating the last key steps of FAO, including *hydroxyacyl-CoA dehydrogenase (HADH)*, was associated with adverse outcome in neuroblastoma (Figure 6A).

To functionally assess the impact of MYCN expression on FAO, we measured OCR in the presence of BSA-coupled palmitate as an exogenous source of fatty acids, and compared with unconjugated BSA as control. Interestingly, MYCN positively regulated the capacity for FAO, because addition of palmitate resulted in a dramatic increase in both basal and maximal respiration rate in the BE(2)sh MYCN ON compared with BE(2) sh MYCN OFF and SH-EP non-MYCN-amplified cells (Figure 6C). These results suggest that MYCN increases the capacity to oxidize exogenous fatty acids. In contrast, all parameters of mitochondrial respiration remained low in non-MYCN-amplified NB cells.

### Inhibition of Fatty Acid $\beta$ -oxidation in MYCN-amplified NB Cells Reduces Tumor Burden

Our results showed that the metabolic phenotype of MYCN-amplified NB cells is characterized by high rates of OXPHOS. In addition, we found that fatty acids greatly contribute to mitochondrial respiration in MYCN-amplified NB cells. Analysis of the Kocak (Kocak et al., 2013) and Versteeg (Molenaar et al., 2012) datasets demonstrated a robust correlation between high expression of the gene encoding the rate-limiting enzyme of FAO, *CPT1C*, with poor prognosis in NB patients (Figures 7A and S7A), suggesting that CPT1 could be an attractive treatment target. To study the effect of FAO inhibition in NB, we treated SK-N-BE(2), SH-EP, and SK-N-AS cells with two different CPT1 inhibitors, etomoxir and teglicar. We observed that the viability of SK-N-BE(2) cells was significantly reduced after seven days with etomoxir or teglicar treatment compared with nontreated cells. In contrast,

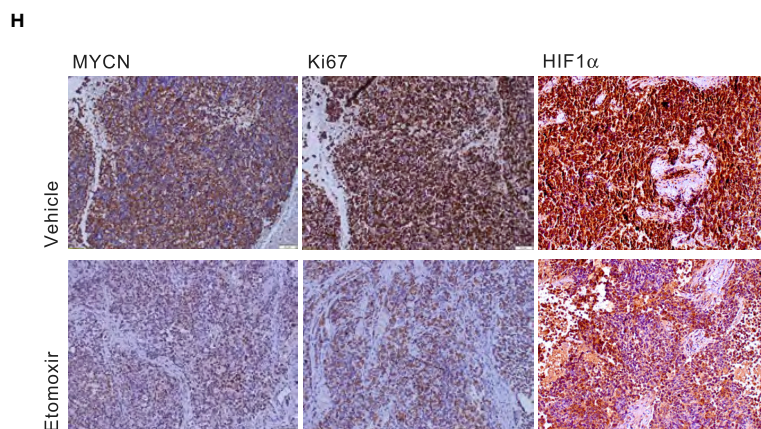
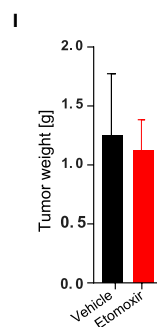
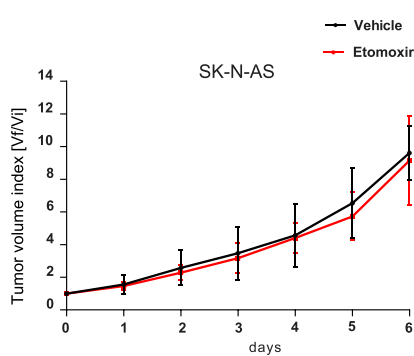
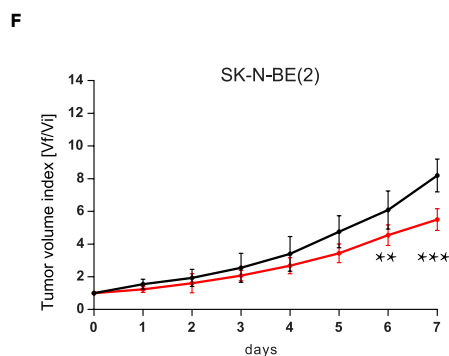
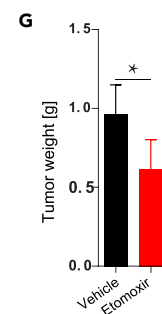
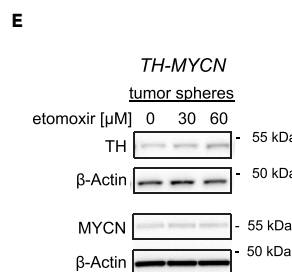
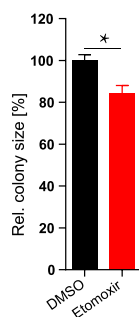
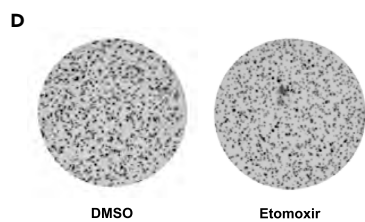
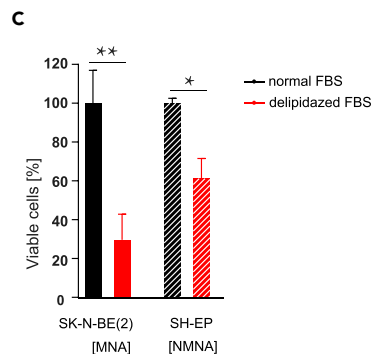
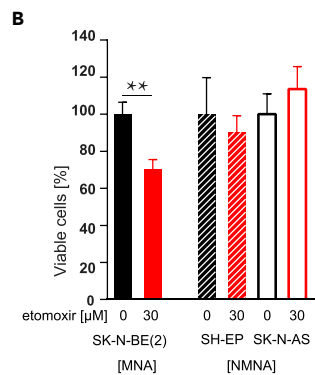
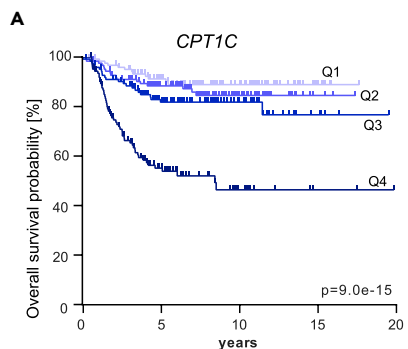


**Figure 7. Inhibition of Fatty Acid  $\beta$ -oxidation Reduces Tumor Burden**

- (A) Kaplan-Meier overall survival curve for the Kocak cohort based on *CPT1C* mRNA expression quartiles (Q1–4).
- (B) Percentage of viable cells as determined by WST-1 assay after seven days of etomoxir treatment in SK-N-BE(2), SH-EP, and SK-N-AS cells.
- (C) Percentage of viable SK-N-BE(2) and SH-EP cells after five days of culturing in substrate-restricted medium as determined by cell counting. All data in B and C are presented as mean  $\pm$  SD from three independent experiments. MNA = MYCN-amplified; NMNA = non-MYCN-amplified.
- (D) Soft agar assay of SK-N-BE(2) after ten days of DMSO or 50  $\mu$ M etomoxir treatment. Representative images from three independent experiments are shown to the left. Quantification of colony size was performed using OpenCFU software, shown to the right.
- (E) Immunoblot showing tyrosine hydroxylase (TH) expression after treatment of TH-MYCN tumor spheres with etomoxir as indicated. Representative blot from three independent experiments is shown.  $\beta$ -actin was used as loading control.
- (F) Tumor volume index (TVI) in xenograft models of SK-N-BE(2) (left panel) and SK-N-AS (right panel) NB cells. NMRI nude mice were treated daily with vehicle (10%  $\beta$ -cyclodextrin) or 20 mg/kg etomoxir. SK-N-BE(2) xenograft: n = 6 for the vehicle group and n = 5 for the etomoxir group, SK-N-AS xenograft: n = 5 for the vehicle group and n = 5 for the etomoxir group. All data are presented as mean  $\pm$  SD.
- (G) SK-N-BE(2) xenograft tumor weights at endpoint. n = 6 for the vehicle group and n = 5 for the etomoxir group. All data are presented as mean  $\pm$  SD.
- (H) Microscopic images of IHC staining of *in vivo* derived tumors labeled with anti-Ki67, anti-MYCN, and anti-HIF1 $\alpha$  antibodies. Representative images from six vehicle and five etomoxir treated SK-N-BE(2) xenograft tumors are shown. Scales bars indicate 50  $\mu$ m.
- (I) SK-N-AS xenograft tumor weights at endpoint. n = 5 for the vehicle group and n = 5 for the etomoxir group. All data are presented as mean  $\pm$  SD, with \*, \*\* indicating p < 0.05 and p < 0.01, respectively. See also Figure S7.

inhibition of  $\beta$ -oxidation did not have any effect on SH-EP or SK-N-AS cells, suggesting that MYCN-amplified cells are more dependent on the FAO pathway (Figures 7B and S7B). We also found that treatment with both compounds resulted in the accumulation of lipid droplets (Figure S7F) according to our previous data on etomoxir (Zirath et al., 2013). In addition, delipidized FBS significantly reduced the number of alive SK-N-BE(2) cells compared with cells in complete FBS, whereas SH-EP cells cultured under the same conditions were less sensitive to the reduction of available lipids in the medium (Figure 7C). Furthermore, we found a significant decrease in size of soft agar colonies formed by SK-N-BE(2) cells upon etomoxir treatment (Figure 7D) and a robust reduction in colony number by teglicar (Figure S7C). In addition, we observed that inhibition of  $\beta$ -oxidation in tumor spheres derived from tumors from the TH-MYCN mouse model resulted in increased expression of the neural differentiation marker tyrosine hydroxylase (TH) (Figure 7E). Together our results indicate the importance of FAO for MYCN-amplified NB proliferation and survival. Next, we analyzed the therapeutic effect of FAO inhibition *in vivo* using two different MYCN-amplified NB cell lines. Nude mice were subcutaneously injected with SK-N-BE(2) or IMR32 cells followed by etomoxir treatment. From day five onwards, we detected a significant decrease in tumor volume index in the treated mice compared with control animals in both experiments (Figures 7F [left panel] and S7D). This result was verified by analysis of tumor weight at endpoint (Figure 7G). Staining of the tumors derived from the *in vivo* experiment demonstrated decreased expression of MYCN, the proliferation marker Ki67, as well as the master regulator of hypoxia signaling, HIF1 $\alpha$ , upon etomoxir treatment (Figure 7H). To analyze any selective effect of CPT-1 inhibition on MYCN-amplified neuroblastoma tumors we next conducted an *in vivo* study using non-MYCN-amplified cells. Nude mice were injected with SK-N-AS cells followed by etomoxir injection. In contrast to the results obtained using SK-N-BE(2) and IMR32 cells, six days of etomoxir treatment did not have any effect on tumor volume index and/or tumor weight of the SK-N-AS tumors (Figure 7F [right panel] and Figure 7I). Staining of the SK-N-AS tumors showed that etomoxir treatment did not impact expression of any of the proteins analyzed (Figure S7G). Together, our data demonstrate that NB cells are differentially sensitive to FAO inhibition depending on their MYCN status.

**DISCUSSION**

During tumor progression, cancer cells need to adjust their metabolic activity in order to maintain high biosynthetic rates needed for rapid cell growth, despite conditions of low nutrient and oxygen availability, and these adaptations are crucial for cancer cell survival. This metabolic rewiring guarantees a rapid energy supply in the form of ATP and a stable source of intermediary metabolites and reducing equivalents needed for the synthesis of new biomass and the control of redox homeostasis (Deberardinis and Chandel, 2016). The relevance of metabolic alterations for tumor biology has resulted in numerous clinical trials based on agents targeting tumor metabolism that have been initiated during the last decade (Luengo et al., 2017). Some of them have already been approved for the treatment of specific tumor types, including the mTOR inhibitor Everolimus for the treatment of metastatic renal cell carcinoma (Polivka and Janku, 2014). The proliferation rate of several malignancies requires high glucose level and may be sensitive to inhibition of glucose transporters (Hay, 2016). The combination of antioxidants or ROS-modulating agents with chemotherapy results in increased efficacy of treatment of patients with neck and head cancer (Kawecki et al., 2007; Shapiro et al., 2005). However, very little is known regarding the metabolic features of

MYCN-amplified tumors, and, specifically, neuroblastoma. Furthermore, to directly target the transcriptional activity of MYC proteins continues to be a major challenge (Dang et al., 2017). Therefore, targeting processes downstream of MYCN could represent a successful approach to inhibit MYCN-driven malignancies. Understanding how MYCN alters the metabolic properties of NB could help to develop novel therapeutic strategies. To explore possible clinical applications of targeting metabolic processes in MYCN-amplified NB requires an accurate and detailed picture of possible metabolic aberrations. Here, we have used the combined information from mRNA and protein expression data, placed into a biological context when integrated with functional analysis, to depict the main metabolic features of this disease. We show that MYCN correlates with metabolic gene and protein expression programs in NB and that MYCN functionally affects major aspects of cell metabolism in NB cells.

Notably, the overlay between proteins and mRNAs not only revealed an overlap between *in vitro* and patient data but also displayed dependency on MYC signaling level. This detailed overview of the MYCN-associated metabolic processes in NB, based on the analysis of gene and protein expression data, allowed us to expose that MYCN-amplified cells and tumors display enhanced expression of proteins and genes involved in glycolysis, OXPHOS, and ROS detoxification. These data provide important clues of the metabolism in MYCN-amplified tumors that could be exploited for the development of therapeutic approaches.

An increased glycolytic flux is a characteristic feature of most cancers and is advantageous mainly because it provides energy during conditions of low oxygen levels and for the generation of chemical building blocks needed for anabolic processes used by cancer cells (Deberardinis and Chandel, 2016). Although previous reports have suggested NB cells and tumors to highly depend on glycolysis for survival and malignancy (Levy et al., 2012; Matsushita et al., 2012), here we could demonstrate for the first time that MYCN enhances OXPHOS in NB cells. It is generally believed that metabolic remodeling is a dynamic process that varies depending on the stage of tumorigenesis (Deberardinis and Chandel, 2016). In this regard, although glycolysis activation is a hallmark of many tumors, there is an increasing appreciation of the importance of mitochondria for cancer cell survival, including the oxidation of substrates such as glucose, glutamine, and fatty acids. In fact, under some circumstances during the tumorigenic process, neoplastic cells may be critically dependent on mitochondria and oxidative phosphorylation rather than on glycolysis (Vyas et al., 2016). There is also evidence for tumors with the capacity to switch between glycolytic and oxidative metabolism under conditions of limiting substrate accessibility, and in response to hypoxia (Deberardinis and Chandel, 2016). As other tumorigenic events, this metabolic adaptation is likely to be a consequence of the actions of oncogenes and tumor suppressors (Nagarajan et al., 2016).

Here we show that neuroblastoma cells rely both on glycolysis and OXPHOS for energy production, but the metabolic program driven by MYCN-amplification seems to depend to a greater extent on OXPHOS. Both OXPHOS capacity and glycolytic rate are significantly reduced following MYCN downregulation in NB cells and are lower in non-MYCN-amplified cells compared with amplified, showing that both pathways are positively associated to MYCN expression. However, simulation of energy demand condition demonstrates the ability of MYCN-amplified cells to increase OXPHOS-dependent ATP production to a greater extent than non-amplified cells. On the contrary, glycolytic parameters are MYCN independent upon stress, as both MYCN-amplified and nonamplified cell lines increased glycolysis to a similar extent. Of importance for possible therapeutic interventions, the analysis of patient gene expression data and proteomics results shows that high MYCN levels are associated with elevated expression of key enzymes involved in glycolysis and the citric acid cycle and with alterations in the levels of respiratory chain proteins. High expression of a vast majority of the corresponding genes correlates to poor survival of NB patients. We analyzed the impact of the expression levels of specific metabolic genes on neuroblastoma patient survival using the Kocak cohort (Kocak et al., 2013), one of the biggest publicly available neuroblastoma datasets covering gene expression data for 649 patients from all five INSS stages of the disease. We validated the results using a second independent dataset (Molenaar et al., 2012) with a similar proportion of MYCN-amplified and non-MYCN-amplified patients as the Kocak cohort and with patient data from the five INSS stages. Our results suggest that targeting these enzymes or pathways could provide therapeutic opportunities for neuroblastoma treatment not explored to date.

Additionally, increasing evidence show that selection of alterations that cause escape from oxidative damage is an important mechanism of metabolic adaptation in tumors (Rodriguez and Vincent, 2018) (Helfinger and Schroder, 2018) and has been linked to chemotherapy resistance in cancer stem cells (Diehn et al., 2009). Among the different functional mitochondrial protein categories and gene programs in our data were

enzymes involved in ROS detoxification, including members of the peroxiredoxin system and those regulating cellular GSH levels. *MYCN*-amplified tumors are likely to have higher energy demand due to increased proliferation rate. Thus, they may compensate the increased ROS production due to increased OXPHOS by upregulation of these ROS detoxification systems required for cell survival.

Fatty acids, glucose, and glutamine are crucial substrates for Krebs cycle function and mitochondrial energy production in many cancer types (Boroughs and Deberardinis, 2015). In fact, nutrient dependency is recognized as a feature of *MYC*-transformed tumors (Dang, 2012). Several studies have demonstrated glutamine addiction of cancer cells driven by *MYC* (Wise et al., 2008; Wise and Thompson, 2010), although *MYC* is also able to induce glutamine synthesis in a mouse model of NSCLC (Yuneva et al., 2012). Here we demonstrate that neuroblastoma cells are able to fuel oxidative metabolism using different substrates, with fatty acids and glucose as the major sources, and with limited contribution of glutamine in *MYCN*-amplified cells. Importantly, these cells are able to perform *de novo* glutamine synthesis based on metabolic tracing experiments showing uptake of U-<sup>13</sup>C<sub>6</sub>-glucose for glutamine synthesis in *MYCN*-amplified cells. In spite of glutamine being the most abundant amino acid in plasma (Smith and Wilmore, 1990), intra-tumoral availability of glutamine might be restricted due to limited vascularization and nutrient diffusion. Notably, *MYCN*-amplified cells are able to survive glutamine starvation and even support cell growth after an initial period of adaptation. Our data may explain the adaptability and high aggressiveness of *MYCN*-driven tumors and provide new information about neuroblastoma biology.

As mentioned above, both glucose and fatty acids are the major substrates for OXPHOS in *MYCN*-amplified neuroblastoma cells. Previous studies have determined the feasibility of targeting glucose utilization as a strategy to treat neuroblastoma (Aminzadeh et al., 2015). Since no previous reports have approached the impact of lipid catabolism in neuroblastoma, here we characterized the therapeutic potential of interfering with fatty acid oxidation in this tumor. Stimulation of FAO can provide a mechanism for survival in the absence of glucose by contributing to cytosolic NADPH levels and ATP supply by OXPHOS (Bellance et al., 2009; Carracedo et al., 2013). We found that *MYCN* is linked to multiple changes in the mRNA and protein expression levels of  $\beta$ -oxidation-associated enzymes. Acyl-CoA dehydrogenases (ACADs) are involved in regulating the first step of fatty acid oxidation. Importantly, protein expression of ACADs were found to correlate inversely to NB patient survival, whereas those enzymes regulating the last key steps of  $\beta$ -oxidation (3-hydroxyacyl-CoA dehydrogenases [HADH] and 3-ketoacyl thiolase [ACAA2]) correlate with poor outcome when highly expressed (Figure 6A). High expression of gene encoding the  $\beta$ -oxidation rate-limiting enzyme CPT-1 also correlates with poor prognosis in NB patients. Hence, based on these observations, the picture of a potential role of  $\beta$ -oxidation in *MYCN*-amplified NB is not clear-cut. However, our results strongly suggest that fatty acids are a major substrate for OXPHOS-based energy metabolism in NB. Interestingly, we found that *MYCN* positively regulates the capacity for oxidizing exogenous fatty acids in NB cells. Furthermore, we showed that reduced availability of extracellular lipids, without any chemical intervention, diminished neuroblastoma cell viability *in vitro*. Together these findings reflect the overall induced OXPHOS capacity of *MYCN*-amplified NB cells, which includes the ability of oxidizing fatty acids. Accordingly, the CPT-1 small molecule inhibitors etomoxir and teglicar were able to reduce *MYCN*-amplified neuroblastoma cell viability and colony formation. Although etomoxir, an irreversible CPT1 inhibitor, has been described to be able to inhibit mitochondrial complex I, this occurs at concentrations much higher than those used in the present study (Yao et al., 2018). Etomoxir reached Phase II clinical trials as an antidiabetic agent before being discontinued due to hepatic toxicity but continues to be widely used as a tool to study FAO in preclinical studies. Teglicar is a recently developed selective and reversible CPT1 inhibitor that also shows antidiabetic activity (Conti et al., 2011). This molecule does not share a similar toxicity profile as etomoxir. While we and others have previously used etomoxir as a tool to inhibit FAO in neuroblastoma cells *in vitro* (Zirath et al., 2013; Nalecz et al., 1997; Zimmermann et al., 2017), we show here for the first time that this FAO-inhibitor is able to reduce *MYCN*-amplified xenograft tumor growth *in vivo*. Importantly, we demonstrate that non-*MYCN*-amplified neuroblastoma tumor growth was not affected by FAO-inhibition, thus showing specificity for *MYCN*-amplification. In this respect it is interesting that  $\beta$ -oxidation of exogenous fatty acids delivered by nearby adipocytes to ovarian cancer cells was shown to be an important mechanism for tumor metastasis and rapid tumor growth (Nieman et al., 2011). The outcome of our *in vivo* study demonstrated the therapeutic potential of FAO inhibition in *MYCN*-amplified NB and suggests that this approach may be used as a basis for the development of novel therapeutic strategies for *MYCN*-amplified NB patients.

Together our data indicate that MYCN facilitates a high-energetic metabolic phenotype in NB, pointing to the possibility that tumors with elevated MYCN signaling have a greater ability than the nonamplified tumors to use different metabolic strategies during tumor progression, depending on microenvironmental and intratumoral nutrient availability and level of metabolic stresses (Jose et al., 2011). Our work highlights several pathways as critical for the aggressive clinical behavior of MYCN-amplified NB tumors. This information can be used to further investigate the importance of these regulatory metabolic networks for MYCN-amplified NB cell survival and as a basis for the development of novel therapies.

### Limitations of the Study

In this study, we performed *in vitro* experiments using the CPT1C inhibitors etomoxir and teglicar, whereas the *in vivo* experiments were limited to etomoxir. As mentioned in the discussion, etomoxir was discontinued from clinical trials due to toxicity and has, at higher concentrations than we employed, unspecific targets such as complex I of the electron transport chain. Future *in vivo* studies with additional CPT1C inhibitors, including teglicar, remain to be performed. Notably, the neuroblastoma cell lines used in our xenograft experiments are highly aggressive and develop tumors rapidly, allowing for a very short therapeutic window of only 7–8 days. Therefore, it may be of importance to use the transgenic TH-MYCN mouse neuroblastoma model in future experiments.

### METHODS

All methods can be found in the accompanying [Transparent Methods supplemental file](#).

### SUPPLEMENTAL INFORMATION

Supplemental Information can be found online at <https://doi.org/10.1016/j.isci.2019.10.020>.

### ACKNOWLEDGMENTS

We are grateful to Professor C. Einvik and Dr. C Løkke (Department of Clinical Medicine, The Arctic University of Norway, Tromsø, Norway) for the BE(2)*sh* MYCN and Kelly *sh*MYCN cell lines, to Professor M. Schwab (German Cancer Research Center, Heidelberg, Germany) for the Tet-21/N cells, and to Professor M. Fischer (Department of Pediatric Oncology and Hematology, University of Cologne, Germany) for generously sharing clinical information. We thank S. Utz for technical assistance, M. Klarqvist and Dr. E. Fredlund for bioinformatic analyses, Dr. K. Hulthenby and the KI TEM core facility for excellent assays, K. Andersson for expert support with animal experiments, Dr. D. Ribeiro for animal expertise, and Dr. N. Vacanti for generously sharing expertise on metabolic tracing assays. We are indebted to Associate Professor M. Wilhelm and all members of the Wilhelm and Arsenian-Henriksson laboratories for fruitful discussions, and to Drs. D. Ribeiro and A. Rodríguez-García for critical reading of the manuscript. This work was supported by grants from the Foundation for Strategic Research (grant number FFL12-0220) to RN and from research grants to MAH from the Swedish Cancer Society, the Swedish Childhood Cancer Fund, the Swedish Research Council, the King Gustaf V Jubilee Fund, and Karolinska Institutet. HZ was recipient of a graduate student grant from KI (KID), MVRP and JD of postdoctoral positions from the Swedish Childhood Cancer Fund, RN of a KI Senior Research Position, and MAH of a Senior Investigator Award from the Swedish Cancer Society.

### AUTHOR CONTRIBUTIONS

GO, MVRP, HZ, and MAH conceived the study. GO, MVRP, LSA, and JD designed and performed cell culture, Western blots, functional metabolic experiments, bioinformatics, mouse studies, and analyzed data together with MAH. GO, MVRP, MAH, HGA, CW, and RN designed, performed, and analyzed metabolomics experiments. GO, MAH, HJJ, and JL designed, performed, and analyzed proteomics experiments. GO, MVRP, HZ, HJJ, and MAH wrote the manuscript. All authors read and commented on the manuscript.

### DECLARATION OF INTERESTS

The authors declare no competing interests.

Received: January 7, 2019

Revised: July 10, 2019

Accepted: October 8, 2019

Published: November 22, 2019

## REFERENCES

- Aminzadeh, S., Vidali, S., Sperl, W., Kofler, B., and Feichtinger, R.G. (2015). Energy metabolism in neuroblastoma and Wilms tumor. *Transl. Pediatr.* **4**, 20–32.
- Bellance, N., Lestienne, P., and Rossignol, R. (2009). Mitochondria: from bioenergetics to the metabolic regulation of carcinogenesis. *Front. Biosci.* **14**, 4015–4034.
- Boroughs, L.K., and Deberardinis, R.J. (2015). Metabolic pathways promoting cancer cell survival and growth. *Nat. Cell Biol.* **17**, 351–359.
- Branca, R.M., Orre, L.M., Johansson, H.J., Granholm, V., Huss, M., Perez-Bercoff, A., Forshed, J., Kall, L., and Lehtio, J. (2014). HiRIEF LC-MS enables deep proteome coverage and unbiased proteogenomics. *Nat. Methods* **11**, 59–62.
- Brodeur, G.M. (2003). Neuroblastoma: biological insights into a clinical enigma. *Nat. Rev. Cancer* **3**, 203–216.
- Carracedo, A., Cantley, L.C., and Pandolfi, P.P. (2013). Cancer metabolism: fatty acid oxidation in the limelight. *Nat. Rev. Cancer* **13**, 227–232.
- Cheung, N.K., and Dyer, M.A. (2013). Neuroblastoma: developmental biology, cancer genomics and immunotherapy. *Nat. Rev. Cancer* **13**, 397–411.
- Conti, R., Mannucci, E., Pessotto, P., Tassoni, E., Carminati, P., Giannessi, F., and Arduini, A. (2011). Selective reversible inhibition of liver carnitine palmitoyl-transferase 1 by teglicar reduces gluconeogenesis and improves glucose homeostasis. *Diabetes* **60**, 644–651.
- Dang, C.V. (2012). MYC on the path to cancer. *Cell* **149**, 22–35.
- Dang, C.V., Reddy, E.P., Shokat, K.M., and Soucek, L. (2017). Drugging the 'undruggable' cancer targets. *Nat. Rev. Cancer* **17**, 502–508.
- Deberardinis, R.J., and Chandel, N.S. (2016). Fundamentals of cancer metabolism. *Sci. Adv.* **2**, e1600200.
- Diehn, M., Cho, R.W., Lobo, N.A., Kalisky, T., Dorie, M.J., Kulp, A.N., Qian, D., Lam, J.S., Ailles, L.E., Wong, M., et al. (2009). Association of reactive oxygen species levels and radioresistance in cancer stem cells. *Nature* **458**, 780–783.
- Fredlund, E., Ringner, M., Maris, J.M., and Pahlman, S. (2008). High Myc pathway activity and low stage of neuronal differentiation associate with poor outcome in neuroblastoma. *Proc. Natl. Acad. Sci. U S A* **105**, 14094–14099.
- Hay, N. (2016). Reprogramming glucose metabolism in cancer: can it be exploited for cancer therapy? *Nat. Rev. Cancer* **16**, 635–649.
- Helfinger, V., and Schroder, K. (2018). Redox control in cancer development and progression. *Mol. Aspects Med.* **63**, 88–98.
- Henriksen, J.R., Haug, B.H., Buechner, J., Tomte, E., Lokke, C., Flaegstad, T., and Einvik, C. (2011). Conditional expression of retrovirally delivered anti-MYC shRNA as an in vitro model system to study neuronal differentiation in MYCN-amplified neuroblastoma. *BMC Dev. Biol.* **11**, 1.
- Hsu, C.L., Chang, H.Y., Chang, J.Y., Hsu, W.M., Huang, H.C., and Juan, H.F. (2016). Unveiling MYCN regulatory networks in neuroblastoma via integrative analysis of heterogeneous genomics data. *Oncotarget* **7**, 36293–36310.
- Huo, L., and Scarpulla, R.C. (2001). Mitochondrial DNA instability and peri-implantation lethality associated with targeted disruption of nuclear respiratory factor 1 in mice. *Mol. Cell. Biol.* **21**, 644–654.
- Jose, C., Bellance, N., and Rossignol, R. (2011). Choosing between glycolysis and oxidative phosphorylation: a tumor's dilemma? *Biochim. Biophys. Acta* **1807**, 552–561.
- Kall, L., Canterbury, J.D., Weston, J., Noble, W.S., and Maccoss, M.J. (2007). Semi-supervised learning for peptide identification from shotgun proteomics datasets. *Nat. Methods* **4**, 923–925.
- Kawecki, A., Adkins, D.R., Cunningham, C.C., Vokes, E., Yagovane, D.M., Dombal, G., Koralewski, P., Hotko, Y., and Vladimirov, V. (2007). A phase II study of ARQ 501 in patients with advanced squamous cell carcinoma of the head and neck. *J. Clin. Oncol.* **25**, 16509.
- Klepinin, A., Chekulayev, V., Timohhina, N., Shevchuk, I., Tepp, K., Kaldma, A., Koit, A., Saks, V., and Kaambre, T. (2014). Comparative analysis of some aspects of mitochondrial metabolism in differentiated and undifferentiated neuroblastoma cells. *J. Bioenerg. Biomembr.* **46**, 17–31.
- Kocak, H., Ackermann, S., Hero, B., Kahlert, Y., Oberthuer, A., Juraeva, D., Roels, F., Theissen, J., Westermann, F., Deubzer, H., et al. (2013). Hox-C9 activates the intrinsic pathway of apoptosis and is associated with spontaneous regression in neuroblastoma. *Cell Death Dis.* **4**, e586.
- Levy, A.G., Zage, P.E., Akers, L.J., Ghisoli, M.L., Chen, Z., Fang, W., Kannan, S., Graham, T., Zeng, L., Franklin, A.R., et al. (2012). The combination of the novel glycolysis inhibitor 3-BrOP and rapamycin is effective against neuroblastoma. *Invest. New Drugs* **30**, 191–199.
- Luengo, A., Gui, D.Y., and Vander Heiden, M.G. (2017). Targeting metabolism for cancer therapy. *Cell Chem. Biol.* **24**, 1161–1180.
- Maris, J.M. (2010). Recent advances in neuroblastoma. *N. Engl. J. Med.* **362**, 2202–2211.
- Matsushita, K., Uchida, K., Saigusa, S., Ide, S., Hashimoto, K., Koike, Y., Otake, K., Inoue, M., Tanaka, K., and Kusunoki, M. (2012). Glycolysis inhibitors as a potential therapeutic option to treat aggressive neuroblastoma expressing GLUT1. *J. Pediatr. Surg.* **47**, 1323–1330.
- Meyer, N., and Penn, L.Z. (2008). Reflecting on 25 years with MYC. *Nat. Rev. Cancer* **8**, 976–990.
- Miller, D.M., Thomas, S.D., Islam, A., Muench, D., and Sedoris, K. (2012). c-Myc and cancer metabolism. *Clin. Cancer Res.* **18**, 5546–5553.
- Molenaar, J.J., Koster, J., Zwijnenburg, D.A., Van Sluis, P., Valentijn, L.J., Van Der Ploeg, I., Hamdi, M., Van Nes, J., Westerman, B.A., Van Arkel, J., et al. (2012). Sequencing of neuroblastoma identifies chromothripsis and defects in neurogenesis genes. *Nature* **483**, 589–593.
- Morrish, F., Neretti, N., Sedivy, J.M., and Hockenbery, D.M. (2008). The oncogene c-Myc coordinates regulation of metabolic networks to enable rapid cell cycle entry. *Cell Cycle* **7**, 1054–1066.
- Muller, I., Larsson, K., Frenzel, A., Oliynyk, G., Zirath, H., Prochownik, E.V., Westwood, N.J., and Henriksson, M.A. (2014). Targeting of the MYCN protein with small molecule c-MYC inhibitors. *PLoS One* **9**, e97285.
- Nagarajan, A., Malvi, P., and Wajapeyee, N. (2016). Oncogene-directed alterations in cancer cell metabolism. *Trends Cancer* **2**, 365–377.
- Nalecz, K.A., Mroczkowska, J.E., Berent, U., and Nalecz, M.J. (1997). Effect of palmitoylcarnitine on the cellular differentiation, proliferation and protein kinase C activity in neuroblastoma nb-2a cells. *Acta Neurobiol. Exp. (Wars)* **57**, 263–274.
- Nieman, K.M., Kenny, H.A., Penicka, C.V., Ladanyi, A., Buell-Gutbrod, R., Zillhardt, M.R., Romero, I.L., Carey, M.S., Mills, G.B., Hotamisligil, G.S., et al. (2011). Adipocytes promote ovarian cancer metastasis and provide energy for rapid tumor growth. *Nat. Med.* **17**, 1498–1503.
- Oberthuer, A., Berthold, F., Warnat, P., Hero, B., Kahlert, Y., Spitz, R., Ernestus, K., Konig, R., Haas, S., Eils, R., Schwab, M., Brors, B., Westermann, F., and Fischer, M. (2006). Customized oligonucleotide microarray gene expression-based classification of neuroblastoma patients outperforms current clinical risk stratification. *J. Clin. Oncol.* **24**, 5070–5078.
- Peifer, M., Hertwig, F., Roels, F., Dreidax, D., Gartlgruber, M., Menon, R., Kramer, A., Roncaioli, J.L., Sand, F., Heuckmann, J.M., et al. (2015). Telomerase activation by genomic rearrangements in high-risk neuroblastoma. *Nature* **526**, 700–704.
- Polivka, J., Jr., and Janku, F. (2014). Molecular targets for cancer therapy in the PI3K/AKT/mTOR pathway. *Pharmacol. Ther.* **142**, 164–175.
- Rodic, S., and Vincent, M.D. (2018). Reactive oxygen species (ROS) are a key determinant of cancer's metabolic phenotype. *Int. J. Cancer* **142**, 440–448.
- Shapiro, G., Supko, J., Ryan, D., Appelman, L., Berkenblit, A., Craig, A., Jones, S., Yagovane, D., Li, C., and Eder, J. (2005). Phase I trial of ARQ 501, an activated checkpoint therapy (ACT) agent, in patients with advanced solid tumors. *J. Clin. Oncol.* **23**, 3042.
- Smith, R.J., and Wilmore, D.W. (1990). Glutamine nutrition and requirements. *J. Parenter. Enteral Nutr.* **14**, 94S–99S.

Vyas, S., Zaganjor, E., and Haigis, M.C. (2016). Mitochondria and cancer. *Cell* *166*, 555–566.

Wise, D.R., Deberardinis, R.J., Mancuso, A., Sayed, N., Zhang, X.Y., Pfeiffer, H.K., Nissim, I., Daikhin, E., Yudkoff, M., McMahon, S.B., and Thompson, C.B. (2008). Myc regulates a transcriptional program that stimulates mitochondrial glutaminolysis and leads to glutamine addiction. *Proc. Natl. Acad. Sci. U S A* *105*, 18782–18787.

Wise, D.R., and Thompson, C.B. (2010). Glutamine addiction: a new therapeutic target in cancer. *Trends Biochem. Sci.* *35*, 427–433.

Yao, C.H., Liu, G.Y., Wang, R., Moon, S.H., Gross, R.W., and Patti, G.J. (2018). Identifying off-target effects of etomoxir reveals that carnitine palmitoyltransferase I is essential for cancer cell proliferation independent of beta-oxidation. *PLoS Biol.* *16*, e2003782.

Yuneva, M.O., Fan, T.W., Allen, T.D., Higashi, R.M., Ferraris, D.V., Tsukamoto, T., Mates, J.M., Alonso, F.J., Wang, C., Seo, Y., et al. (2012). The metabolic profile of tumors depends on both the responsible genetic lesion and tissue type. *Cell Metab.* *15*, 157–170.

Zimmermann, L., Moldzio, R., Vazdar, K., Krewenka, C., and Pohl, E.E. (2017). Nutrient deprivation in neuroblastoma cells alters 4-hydroxynonenal-induced stress response. *Oncotarget* *8*, 8173–8188.

Zirath, H., Frenzel, A., Oliynyk, G., Segerstrom, L., Westermark, U.K., Larsson, K., Munksgaard Persson, M., Hultenby, K., Lehtio, J., Einvik, C., et al. (2013). MYC inhibition induces metabolic changes leading to accumulation of lipid droplets in tumor cells. *Proc. Natl. Acad. Sci. U S A* *110*, 10258–10263.

**ISCI, Volume 21**

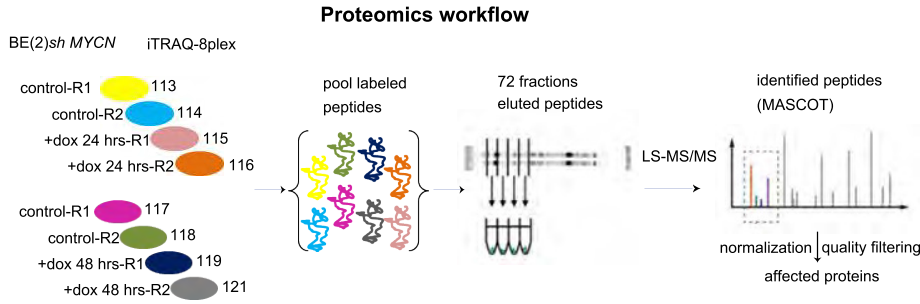
**Supplemental Information**

**MYCN-enhanced Oxidative  
and Glycolytic Metabolism Reveals  
Vulnerabilities for Targeting Neuroblastoma**

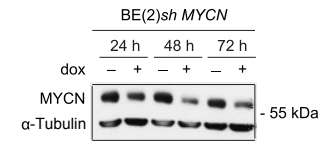
**Ganna Oliynyk, María Victoria Ruiz-Pérez, Lourdes Sainero-Alcolado, Johanna Dzieran, Hanna Zirath, Héctor Gallart-Ayala, Craig E. Wheelock, Henrik J. Johansson, Roland Nilsson, Janne Lehtiö, and Marie Arsenian-Henriksson**

Supplemental Figure 1

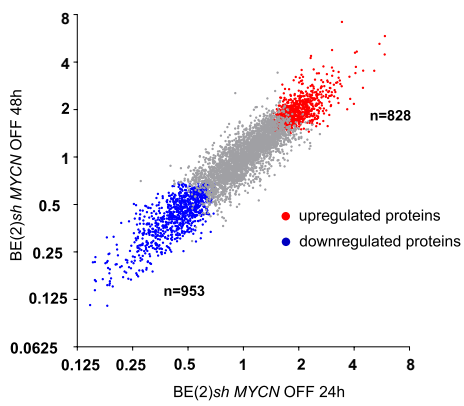
**A**



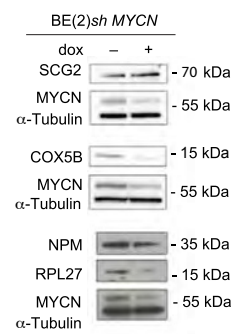
**B**



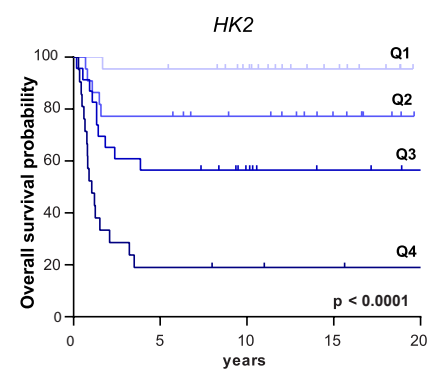
**C**



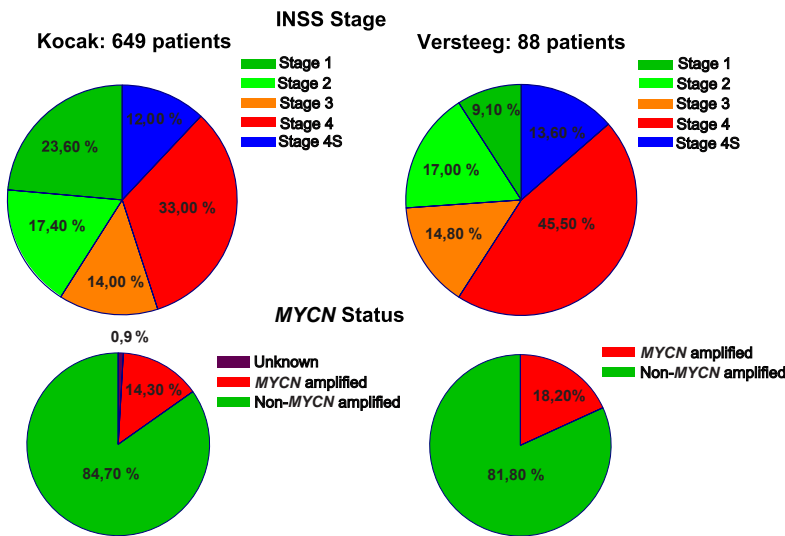
**D**



**F**



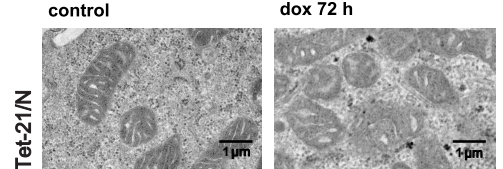
**E**



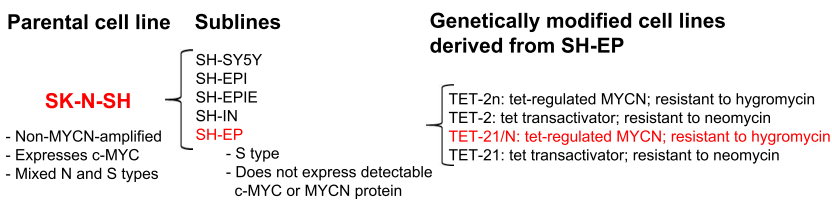
**H**



**I**



**G**



**J**

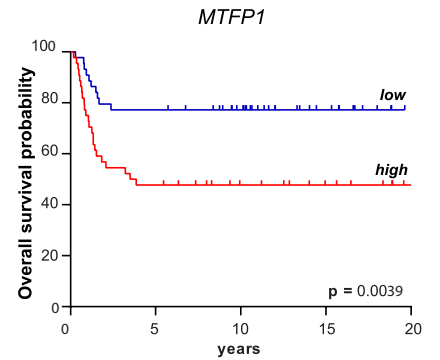
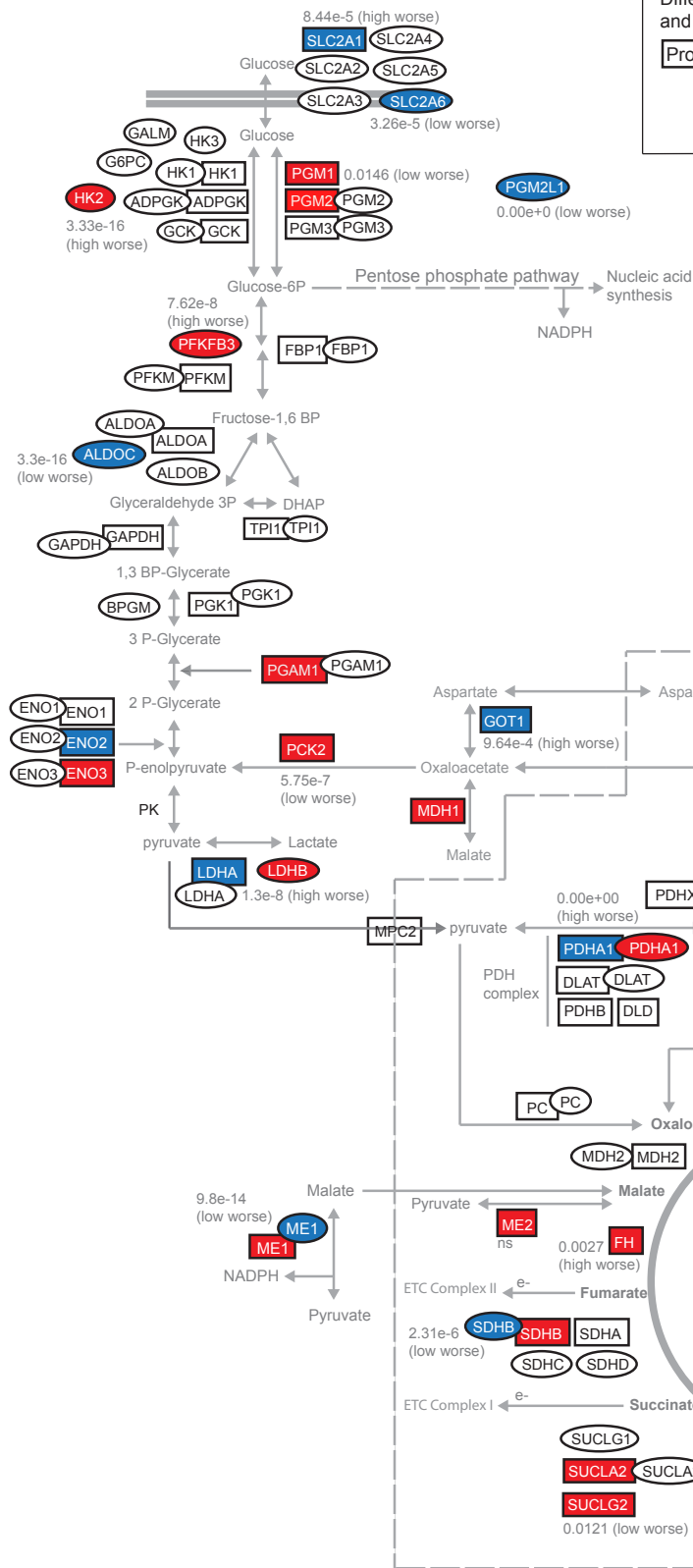


**Figure S1. Related to Figure 1 and Figure 2. Outline of proteomics experiments, validation of downregulation of MYCN following doxycycline treatment and patient survival analysis.** (A) Schematic workflow of the high-resolution quantitative proteomics approach. (B) Immunoblot showing MYCN expression after treatment of BE(2)*sh* MYCN cells with 2 µg/mL doxycycline (dox) for the indicated time points. Representative blot from three independent experiments is shown. (C) Unsupervised clustering of proteins passing initial quality control at 24 and 48 h compared to non-treated BE(2)*sh* MYCN cells. (D) Immunoblot analysis of selected proteins indicated up- or downregulated in the proteomic data after 24 h of MYCN downregulation. Representative blots from two or three independent experiments are shown.  $\alpha$ -Tubulin was used as loading control. (E) Summary of the proportion of patients belonging to each INSS stage and MYCN-amplification status in the two patient datasets used for survival analyses in this study (Kocak *et al.*, 2013 (Molenaar *et al.*, 2012)). (F) Kaplan-Meier plot showing overall survival of neuroblastoma patients based on *HK2* mRNA levels subdivided into expression quartiles (Q1-4). Data from the Versteeg dataset (Molenaar *et al.*, 2012). (G) Scheme summarizing the origin of the MYCN-overexpressing Tet-21/N cell line from a subclone of the non-MYCN-amplified SK-N-SH cell line, adapted from (Thiele, 1998). (H) Immunoblot showing MYCN expression after treatment of Kelly *sh*MYCN and Tet-21/N cells with 2 µg/mL doxycycline (dox) for the indicated time points. The blot shown is representative from three independent experiments. (I) Transmission electron microscopy images of representative mitochondria in Tet-21/N cells. Cells were treated with vehicle or 2 µg/mL doxycycline for 72 h, as indicated. Scale bars represent 1 µm. (J) Kaplan-Meier overall survival curve from the Versteeg cohort based on mRNA expression of the *MTFP1* gene.

Supplemental Figure 2

Glycolysis and Gluconeogenesis



Differential levels of proteins in BE(2)shMYCN ON cells and mRNAs in patient cohort

Protein	mRNA	Upregulated
		Downregulated
		Unchanged

Fatty acid biosynthesis (Lipogenesis)

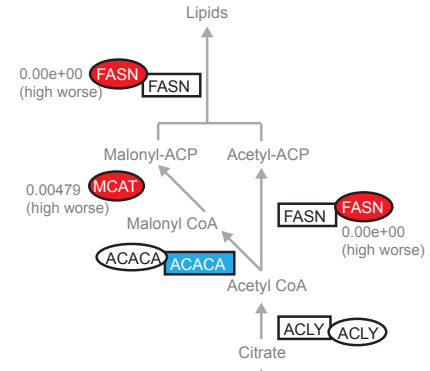


**Figure S2. Related to Figure 2. MYCN-regulated mRNA and protein expression alterations of central metabolic pathways.** Schematic picture showing significantly regulated mRNAs and proteins of the glycolysis/gluconeogenesis, TCA cycle and fatty acid biosynthesis pathways, based on Kyoto Encyclopedia of Genes and Genomes (KEGG) pathway maps ([www.genome.jp/kegg/](http://www.genome.jp/kegg/)). Red and blue colors represent, up- or downregulated mRNAs (ovals) in *MYCN*-amplified versus non-*MYCN* amplified tumors, or proteins (rectangles) in BE(2)sh *MYCN* ON versus BE(2) sh *MYCN* OFF cells. The correlation of expression of different genes (high or low) to patient survival using the Oberthuer patient dataset (Oberthuer *et al.*, 2006) is indicated. ns= not statistically significant.

Supplemental Figure 3

Electron Transport Chain

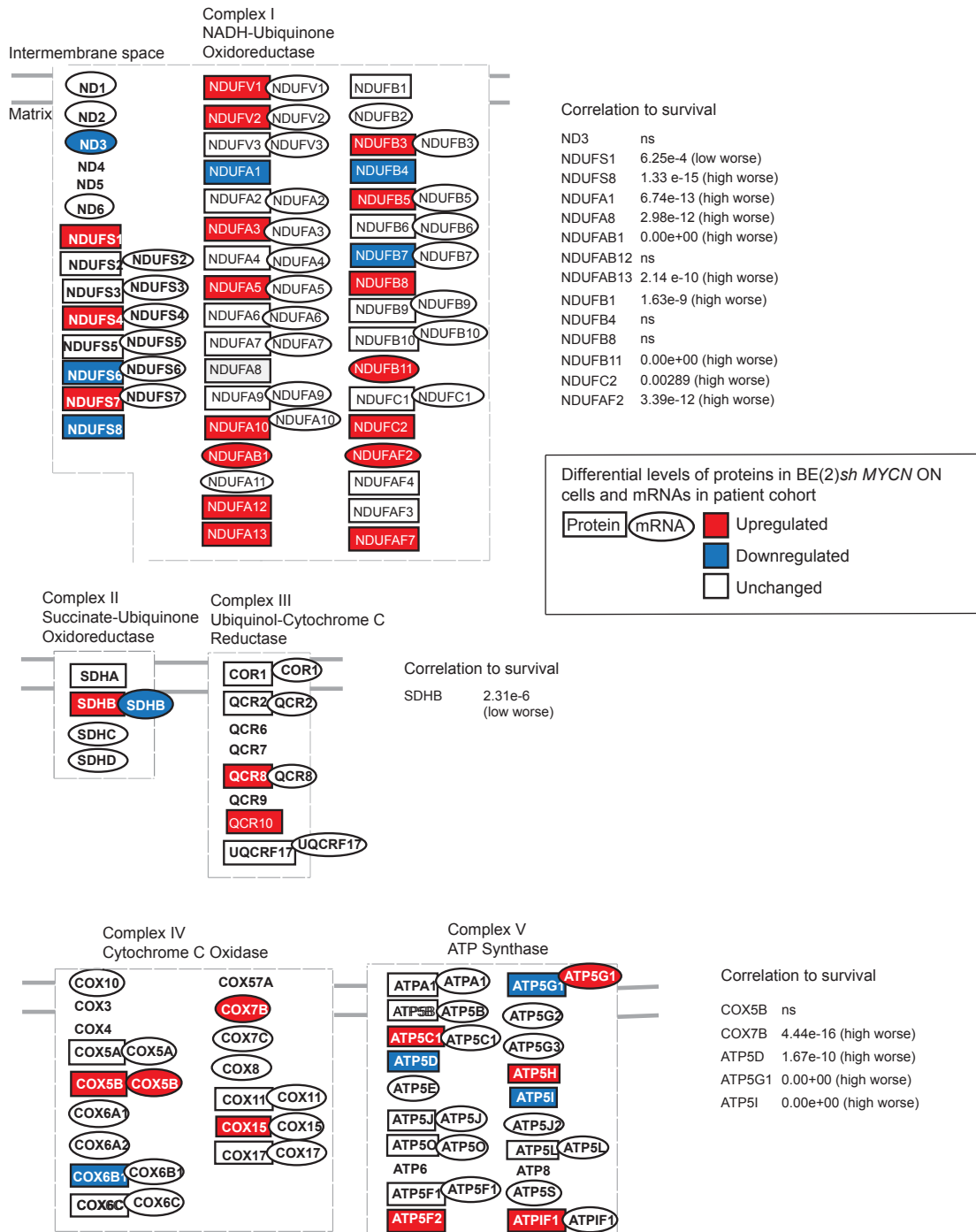
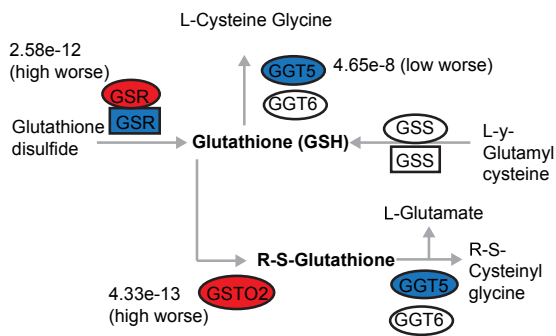


**Figure S3. Related to Figure 2. MYCN-regulated mRNA and protein expression alterations of the respiratory chain.** Schematic picture showing significantly regulated mRNAs and proteins of the respiratory chain, based on KEGG pathway maps. Red and blue colors represent, up- or downregulated mRNAs (ovals) in *MYCN*-amplified versus non-*MYCN* amplified tumors, or proteins (rectangles) in BE(2)sh *MYCN* ON versus BE(2) sh *MYCN* OFF cells. The correlation of expression of different genes (high or low) to patient survival using the Oberthuer patient dataset (Oberthuer *et al.*, 2006) is indicated. ns= not statistically significant.

Supplemental Figure 4

A

Glutathione metabolism



Differential levels of proteins in BE(2)sh MYCN ON cells and mRNAs in patient cohort

Protein	mRNA	Upregulated
		Downregulated
		Unchanged

C

ROS detoxification enzymes

- Glutathione reductase **GSR** **GSR** 2.58e-12 (high worse)
- Glutathione peroxidase 1 **GPX1** ns
- Glutaredoxin 3 **GLRX3** 1.85e-14 (high worse)
- Glutathione S-Transferase Omega **GSTO2** 4.33e-13 (high worse)
- Glutathione S-transferase mu **GSTM3**
- Glutathione S-transferase pi 1 **GSTP1** 0.00111 (high worse)
- Glutathione S-transferase zeta 1 **GSTZ1** 2.22e-16 (high worse)
- Glutathione S-transferase kappa 1 **GSTK1** **GSTK1** 1.29e-6 (low worse)
- Microsomal glutathione S-transferase 2 **MGST2** ns

- Peroxiredoxin 1 **PRDX1** ns
- Peroxiredoxin 2 **PRDX2** 1.21e-10 (high worse)
- Peroxiredoxin 3 **PRDX3** 3.85e-6 (high worse)
- Peroxiredoxin 4 **PRDX4** 0.00e+00 (high worse)
- Peroxiredoxin 6 **PRDX6** **PRDX6** 4.44e-16 (high worse)
- Catalase **CAT** ns
- Thioredoxin **TXN** 6.72e-5 (high worse)
- Thioredoxin-related transmembrane protein 1 **TMX1** no info
- Thioredoxin-related transmembrane protein 2 **TMX2** no info
- Thioredoxin-related transmembrane protein 3 **TMX3** no info

B

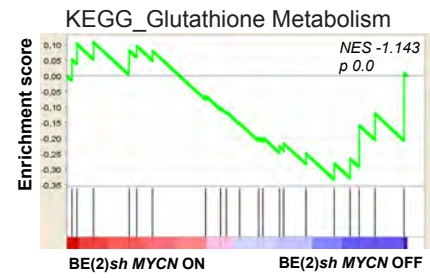


**Figure S4. Related to Figure 2. MYCN regulated mRNA and protein expression of antioxidant detoxification pathways.** (A) Schematic picture showing significantly regulated mRNAs and proteins involved in glutathione metabolism, based on KEGG pathway maps. Red and blue colors represent, up- or downregulated mRNAs (ovals) in *MYCN*-amplified versus non-*MYCN* amplified tumors, or proteins (rectangles) in BE(2)sh *MYCN* ON versus BE(2) sh *MYCN* OFF cells. The correlation of expression of different genes (high or low) to patient survival using the Oberthuer patient dataset (Oberthuer *et al.*, 2006) is indicated. ns= not statistically significant. (B) KEGG glutathione metabolism enrichment plot (using c2.cp.kegg.v5.2.symbols.gmt gene set obtained from the KEGG pathway database) in BE(2)sh *MYCN* ON versus BE(2)sh *MYCN* OFF cells. (C) List of enzymes involved in antioxidant scavenger pathways. Symbols and color code as in (A).

Supplemental Figure 5

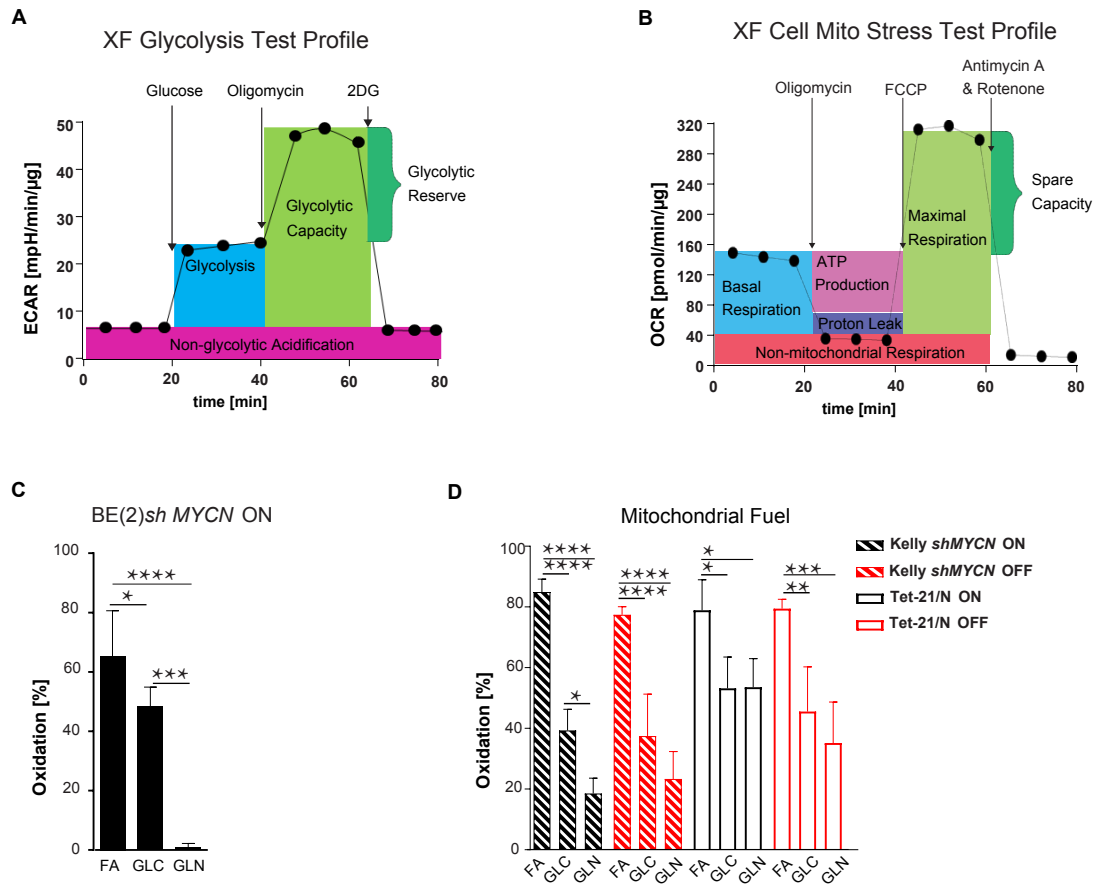


**Figure S5. Related to Figure 3 and Figure 4. Effect of MYCN downregulation on glycolysis and respiration in MYCN-amplified NB cells.** (A) Illustration of the principle of the Glycolysis Stress assay (adapted from Agilent Seahorse XF technology). Extracellular Acidification Rate (ECAR) was measured using a Seahorse Extracellular Flux Analyzer XFe96. Glycolysis is defined by the ECAR measured after addition of 10 mM glucose minus the basal ECAR. Glycolytic capacity is the maximal ECAR measured in response to addition of 1  $\mu$ M oligomycin (ATP synthase inhibitor) minus the non-glycolytic acidification. The difference between glycolytic capacity and glycolysis is defined as the glycolytic reserve. (B) Illustration of the principle of the XF Cell Mito Stress assay (adapted from Agilent Seahorse XF technology). ATP production is defined as the difference between the basal OCR and the OCR after addition of 1  $\mu$ M oligomycin. The maximal respiration consists of the OCR measured in response to addition of 2  $\mu$ M FCCP. The reserve capacity is the difference between maximal respiration and basal OCR. (C) Quantification of OCR in BE(2)*sh* MYCN ON cells, the same data as used in Figure 4A. (D) Quantification of OCR in Kelly *sh*MYCN and Tet-21/N cells as indicated. FA = fatty acids, GLC = glucose, GLN = glutamine. All data is presented as the mean  $\pm$  SD of three independent experiments, with \*, \*\*, \*\*\*, \*\*\*\* indicating  $p < 0.05$ ,  $p < 0.01$ ,  $p < 0.001$  and  $p < 0.0001$ , respectively.

Supplemental Figure 6

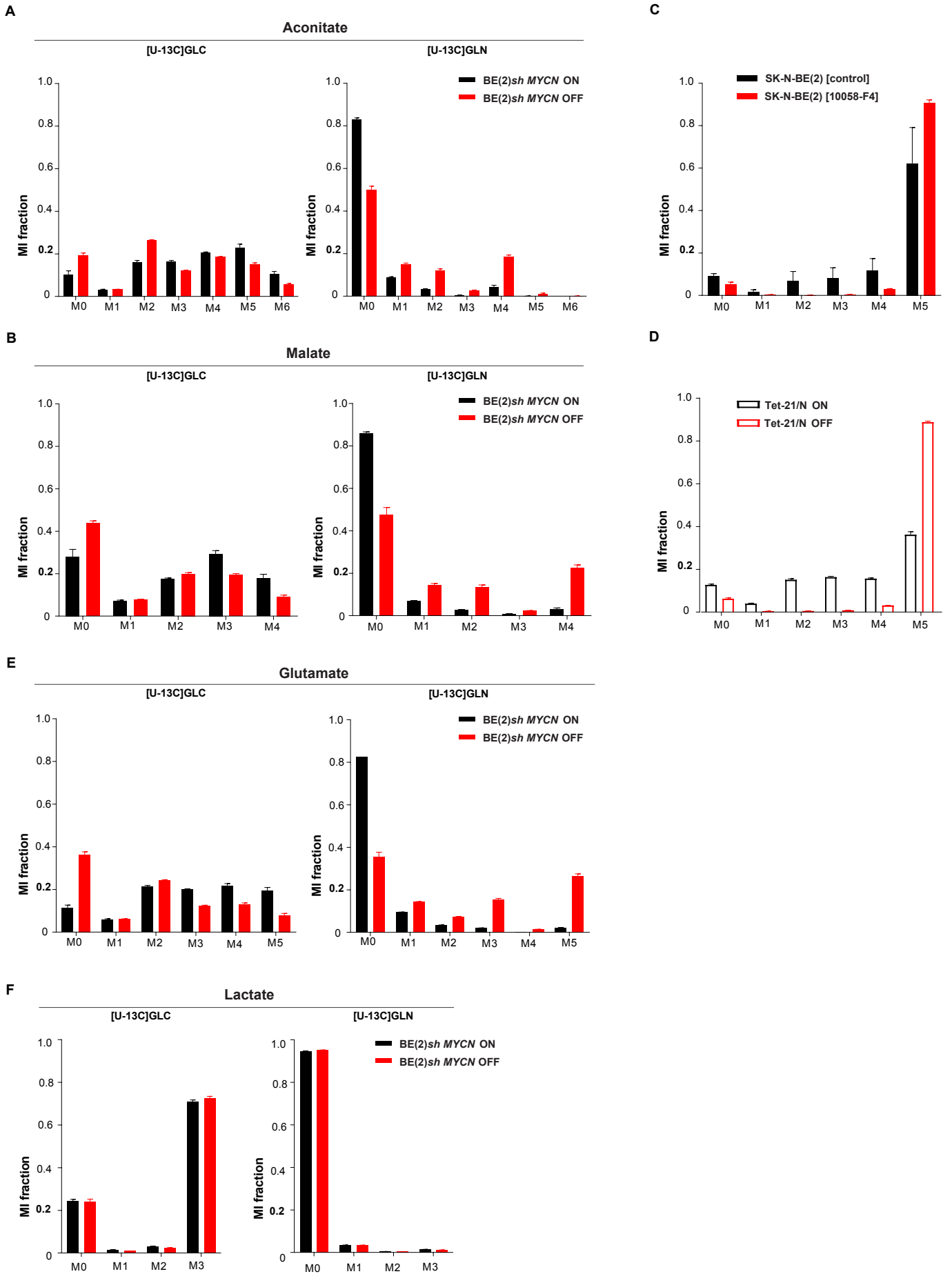


**Figure S6. Related to Figure 5. Distribution of TCA metabolites. (A-D)** The contribution of glucose and glutamine towards TCA-cycle metabolites was measured by metabolic tracing using U-<sup>13</sup>C<sub>6</sub>-glucose and U-<sup>13</sup>C<sub>5</sub>-glutamine. Comparison of mass isotopologue distributions (MID) of aconitate (**A**), malate (**B**), glutamine (**C, D**), glutamate (**E**), and lactate (**F**). The carbon tracing was performed in BE(2)*sh* MYCN ON, BE(2)*sh* MYCN OFF, Tet-21/N ON, Tet-21/N OFF, and SK-N-BE(2) cells after five days of MYCN inhibition by doxycycline or 10058-F4. MI of labeled carbons as indicated (M0-M6).

Supplemental Figure 7

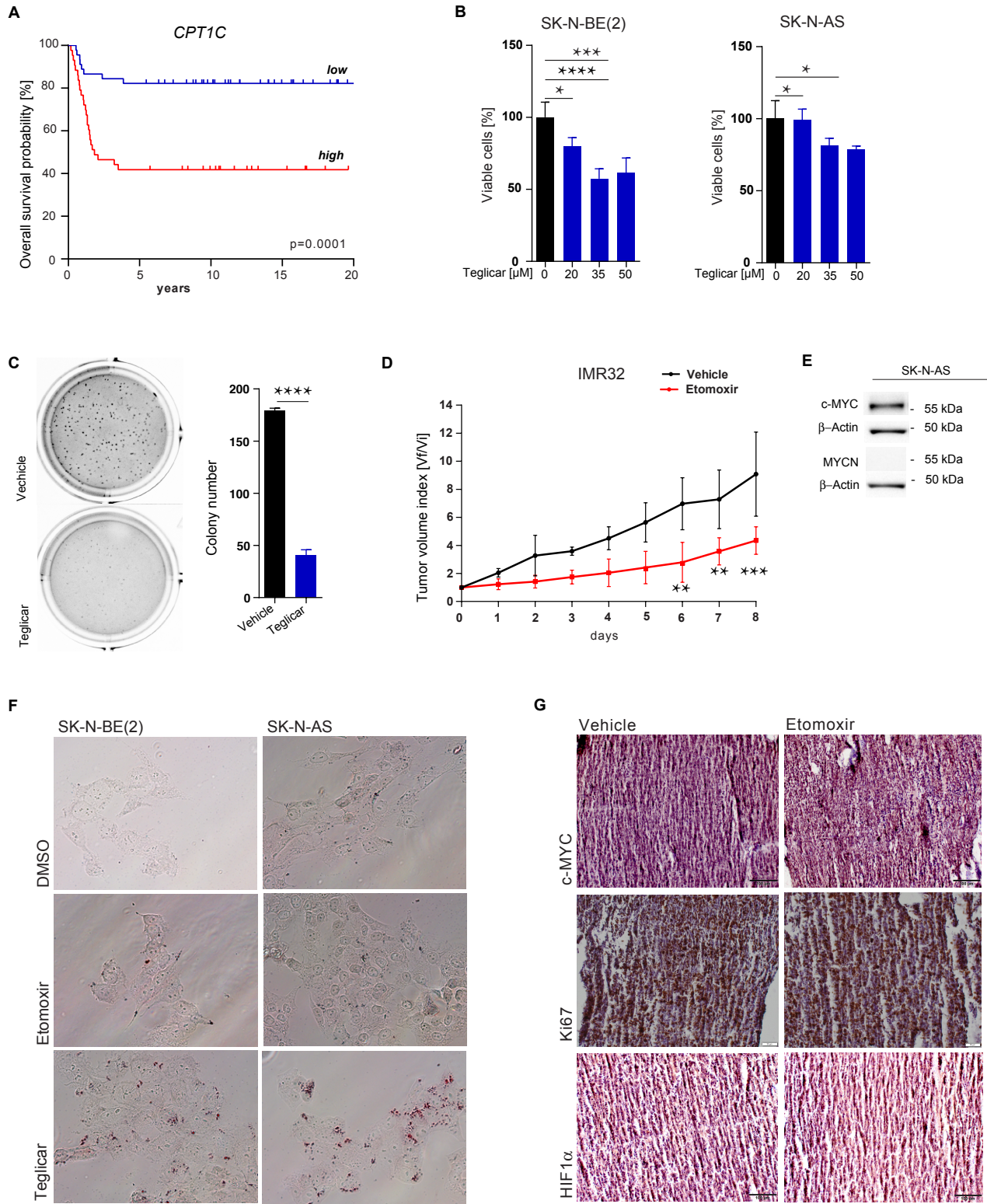


**Figure S7. Related to Figure 7. Inhibition of fatty acid  $\beta$ -oxidation reduces tumor burden.** (A) Kaplan-Meier overall survival curve from the Versteeg cohort based on *CPT1C* mRNA expression. (B) Percentage of viable cells as determined by WST-1 assay after seven days of teglicar treatment at the indicated concentrations in SK-N-BE(2) and SK-N-AS cells. (C) Soft agar assay of SK-N-BE(2) after ten days of vehicle ( $H_2O$ ) or 50  $\mu M$  teglicar treatment. Representative images from three independent experiments are shown to the left. Quantification of colony number was performed using OpenCFU software, shown to the right. (D) Tumor volume index (TVI) in xenograft models of IMR32 NB cells. NMRI nude mice were treated daily with vehicle (10 %  $\beta$ -cyclodextrin) or 20 mg/kg etomoxir.  $n = 3$  for the vehicle (10 %  $\beta$ -cyclodextrin) group and  $n = 4$  for the etomoxir group. All data is presented as mean  $\pm$  SD. (E) Immunoblot showing c-MYC and MYCN expression in SK-N-AS NB cells. Representative blot from three independent experiments is shown.  $\beta$ -actin was used as loading control. (F) Microscopic images of ORO staining of SK-N-BE(2) and SK-N-AS cells treated with vehicle (DMSO) or 50  $\mu M$  etomoxir or teglicar. Representative images are shown. (G) Microscopic images of IHC staining of *in vivo* derived SK-N-AS tumors labelled with anti-Ki67, anti-c-MYC, and anti-HIF1 $\alpha$  antibodies. Representative images from five vehicle treated and five etomoxir treated SK-N-AS-xenograft tumors are shown. Scale bars represent 100  $\mu m$ . All data is presented as mean  $\pm$  SD, with \*, \*\*, \*\*\*, \*\*\*\* indicating  $p < 0.05$ ,  $p < 0.01$ ,  $p < 0.001$  and  $p < 0.0001$ , respectively.

**Supplemental Table 3.** Metabolic proteins differently up- or downregulated in BE(2)sh *MYCN* cells in response to doxycycline treatment (2 µg/mL) where the corresponding genes were present in the *MYCN*-target gene set reported by (Hsu et al., 2016). Up- and downregulated genes as indicated.

**Related to Figure 1 and Figure S1.**

<b>Gene Symbol</b>	<b>Regulation direction by MYCN (Hsu et al., 2016)</b>	<b>Regulation direction by shMYCN</b>
AHCY	Activation	Downregulation
ANXA1	Repression	Upregulation
BOP1	Activation	Downregulation
CCNA2	Activation	Downregulation
CCNB1	Activation	Downregulation
CLIC3	Repression	Upregulation
CSRP1	Repression	Upregulation
DDX1	Activation	Downregulation
DHX33	Activation	Downregulation
EEF1B2	Activation	Downregulation
ELMO2	Repression	Upregulation
EPB41L1	Repression	Upregulation
EXOSC5	Activation	Downregulation
FASN	Activation	Downregulation
FLAD1	Activation	Downregulation
JAK1	Repression	Upregulation
KIAA0319L	Repression	Upregulation
KIF15	Activation	Downregulation
LMBRD1	Repression	Upregulation
LSM7	Activation	Downregulation
MACF1	Repression	Upregulation
MAP1A	Repression	Upregulation
MRPL12	Activation	Downregulation
MRPL4	Activation	Downregulation
MTHFD1L	Activation	Downregulation
MTHFD2	Activation	Downregulation
NCAPG	Activation	Downregulation
NPM1	Activation	Downregulation
NTHL1	Activation	Downregulation
PEX14	Repression	Upregulation
PJA2	Repression	Upregulation
PNPLA8	Repression	Upregulation
PRDM2	Repression	Upregulation
PRDX	Activation	Downregulation
PRDX2	Activation	Downregulation
PRMT1	Activation	Downregulation

PSAT1	Activation	Downregulation
PXN	Repression	Upregulation
S100A13	Repression	Upregulation
SDF4	Repression	Upregulation
SLC16A1	Activation	Downregulation
SNRPG	Activation	Downregulation
SQSTM1	Repression	Upregulation
TMEM222	Repression	Upregulation
TOM1L2	Repression	Upregulation
TOMM20	Activation	Downregulation
WDR12	Activation	Downregulation
YARS2	Activation	Downregulation

## TRANSPARENT METHODS

### CONTACT FOR REAGENT AND RESOURCE SHARING

Further information and requests for resources and reagents should be directed to and will be fulfilled by Lead Contact, Marie Arsenian Henriksson (marie.arsenian.henriksson@ki.se).

### EXPERIMENTAL MODEL AND SUBJECT DETAILS

#### Animal studies

Five-week-old female NMRI-*Foxn1<sup>nu</sup>* mice purchased from Taconic Biosciences were housed, treated, and analyzed in accordance with the ethical permit number N71/15 approved by the Swedish ethical committee "Stockholms Norra Djurförsöksetiska Nämnd". Mice were housed in specific pathogen free conditions where light, temperature (21°C), and relative humidity (50-60 %) were controlled. Food and water were available *ad libitum*. For xenograft experiments,  $10 \times 10^6$  SK-N-BE(2), IMR32, or SK-N-AS cells were injected subcutaneously into the right flanks of mice. Tumor growth was monitored daily by caliper measurement of two dimensions. The tumor volume  $0.1 \text{ cm}^3$  was defined as tumor take point and animals were randomized into the treatment groups. The mice received vehicle (10 % 2-(hydroxypropyl)- $\beta$ -cyclodextrin in  $\text{H}_2\text{O}$ , referred to as  $\beta$ -cyclodextrin) or 20 mg/kg etomoxir by *i.p.* injection daily. The animals were euthanized after six to eight days of treatment or after tumors reached  $1 \text{ cm}^3$ . The procedures for performing all animal experiments were in accordance with the principles and guidelines of Karolinska Institutet and the Swedish law.

#### TH-MYCN tumor spheres

For generation of TH-MYCN-derived spheres, tumors from homozygous mice, both male and female, were cut into small pieces and mechanically dissociated. The resulting cell suspension was washed with PBS twice and filtered through a  $70 \mu\text{m}$  nylon membrane. To remove blood cells, the cell suspensions were treated with red blood lysis buffer (Sigma), followed by a PBS wash. For proliferation, cells were plated at a density of  $5 \times 10^5$  cells/ $\text{cm}^2$  on non-coated or non-adherent tissue culture flasks (Gao *et al.*, 2014; (Ribeiro *et al.*, 2016).

#### Cell culture

The human *MYCN*-amplified NB cell lines SK-N-BE(2) (from male origin), BE(2)sh *MYCN*, Kelly sh*MYCN* (from female origin), expressing a doxycycline inducible *MYCN* shRNA, BE(2)sh Scramble, Tet-21/N (from female origin) overexpressing a doxycycline repressible *MYCN* gene (FS1G) and non-*MYCN*-amplified NB cell lines SK-N-SH (from female origin), SH-EP (from female origin), SK-N-AS (from female origin) as well as the mouse neuroblastoma Neuro-2A cells (from male origin) were grown in MEME:Nutrient Mixture F-12 (1:1) medium containing 1 % non-essential amino acids (NEAA), 1 % GlutaMAX (Gibco) and 1 % penicillin-streptomycin. Human *MYCN*-amplified IMR32 cells (from male origin) were grown in low glucose DMEM supplemented as described above. For small hairpin (sh)-transduced cell lines, the cell culture medium was supplemented with 10 % tetracycline-approved FBS (Clontech), all other cells were grown in regular 10 % FBS (Clontech) (Henriksen *et al.*, 2011). Cell culture media, antibiotics and cell culture supplements were obtained from Sigma-Aldrich. Delipidized fetal bovine serum was from Pan Biotech. Doxycycline and the small molecule *MYCN*-inhibitor 10058-F4 were from Sigma-Aldrich.

## METHOD DETAILS

### Protein extraction, digestion and iTRAQ labelling of peptides

BE(2)sh *MYCN* cells treated with vehicle or 2  $\mu\text{g}/\text{mL}$  doxycycline for 24 or 48 h were lysed in 4 % SDS, 25 mM HEPES, and 1 mM DTT. Cell lysates were heated to 95°C for 5 min followed by sonication for 1 min and centrifugation at  $14 \times 10^3 \text{ g}$  for 15 min, discarding the pellet. Protein concentration was quantified using the DC protein assay (BioRad Laboratories, Hercules, CA, USA). Equal aliquots (100  $\mu\text{g}$ ) of total protein lysates were mixed with 1 mM DTT, 8 M urea, 25 mM HEPES, pH 7.6 and transferred to a centrifugation filtering unit, 10 kDa cutoff (Microcon YM-10, Millipore), and centrifuged for 15 min,  $14 \times 10^3 \text{ g}$ , followed by addition of 8 M urea with 1 mM DTT buffer and centrifuged for 15 min at  $14 \times 10^3 \text{ g}$ . Proteins were alkylated with 50 mM indole acetic acid in 8 M urea, 25 mM HEPES for 10 min,

centrifuged for 15 min,  $14 \times 10^3$  g, followed by two cycles of resuspension in 4 M urea, 25 mM HEPES and centrifugation for 15 min at  $14 \times 10^3$  g. Trypsin (modified sequencing grade, Promega, Madison, WI, USA) (1:50, trypsin:protein) in 250 mM urea, 50 mM HEPES was added to cell lysates and incubated overnight at 37°C. Filter units with 10 kDa cutoff (Microcon YM-10, Millipore) were centrifuged for 15 min,  $14 \times 10^3$  g, followed by another centrifugation with Milli-Q H<sub>2</sub>O and the flow-through was collected. Labeling with iTRAQ (Applied Biosystems, Foster City, CA, USA) was performed according to manufacturer's instructions. Briefly, each iTRAQ reagent was incubated with the protein digest for 2 h, pooled and acidified with formic acid. Excess reagent and detergents were removed from the pooled samples using a SCX-cartridge (strata-X-C, Phenomenex, Torrance, CA, USA). iTRAQ labelled peptides were separated by IPG-IEF on a pH 3.7-4.9 strip.

### **IPG-IEF of peptides**

400 µg of iTRAQ labeled tryptic peptides were dissolved in 8 M urea. Narrow range IPG-strips for isoelectric focusing (pH 3.5–4.9 24 cm long) were kindly supplied by GE Healthcare Bio-Sciences AB, Uppsala, Sweden. Application gels were rehydrated overnight in 8 M urea and 1 % Pharmalyte 2.5–5 (GE Health-care Bio-Sciences AB). Isoelectric focusing was performed on an Ettan IPGphor (GE Healthcare Bio-Sciences AB) with a 75 µA limit per strip until 100 kVh had been reached. Peptides were extracted by a prototype liquid handling robot, supplied by GE Healthcare Bio-Sciences AB, dried in Speedvac and dissolved in 3 % acetonitrile (ACN), 0.1 % formic acid (FA).

### **Liquid chromatography coupled to tandem mass spectrometry (nano LC-MS/MS)**

Peptides were separated using an Agilent 1200 nano-LC system. Samples were trapped on Zorbax 300SB-C18, 5 µm, 5 x 0.3 mm and separated on a NTCC-360/100-5-153 (Nikkyo Technos., Ltd) column using a gradient of A (3 % ACN, 0.1 % FA) and B (95 % ACN, 0.1 % FA), ranging from 3 % to 40 % B in 90 min with a flow of 0.4 µl/min. The LTQ Orbitrap Velos was operated in data dependent mode, selecting 5 precursors for sequential fragmentation by CID and HCD, and analyzed by the linear ion trap and orbitrap, respectively. Survey scan was performed in the orbitrap at  $30 \times 10^3$  resolutions from 300-2,000 *m/z*, using lock mass at *m/z* 445.120025, with a max injection time of 500 ms and AGC set to  $1 \times 10^6$  ions. For generation of HCD fragmentation spectra, a max ion injection time of 500 ms and AGC of  $5 \times 10^4$  were used before fragmentation at 37.5 % normalized collision energy (NCE), 30 ms activation time. For FTMS MS<sub>n</sub> spectra, normal mass range was used, centroiding the data at 7,500 resolution. Peptides for CID were accumulated for a max ion injection time of 200 ms and AGC of  $3 \times 10^4$ , fragmented with 35 % collision energy, wideband activation on, activation q 0.25, activation time 10 ms before analysis at normal scan rate and mass range in the linear ion trap. Precursors were isolated with a width of 2 *m/z* and put on the exclusion list for 60 s. Single and unassigned charge states were rejected from precursor selection.

### **Peptide and protein identification**

Proteome Discoverer 1.3 (Thermo Scientific) using the SEQUEST search engine and Percolator (Kall et al., 2007) was used for protein identification. Precursor mass tolerance was set to 10 ppm and for fragments 0.8 Da and 0.02 Da were used for detection in the linear ion trap and the orbitrap, respectively. Oxidized methionine and phosphorylation on S, T and Y was set as dynamic modifications, and carbamidomethylation, N-terminal 8plex iTRAQ, as fixed modifications. Spectra were matched to Ensembl 68, limited to human protein sequences, and results were filtered to 1 % FDR.

### **Liquid Chromatography – High Resolution Mass Spectrometry (LH-HRMS)**

After 5 days of MYCN inhibition with 2 µg/mL doxycycline, metabolite extracts were analyzed by liquid chromatography – high resolution mass spectrometry (LC-HRMS) on a Thermo Ultimate 3000 UHPLC system coupled to a Q-Exactive Orbitrap mass spectrometer (Thermo Fisher Scientific, San Jose, CA, USA). Metabolites chromatographic separation was performed in a Merck-Sequnt ZIC-HILIC column (150 x 4.6 mm, 5µm particle size) fitted with a Merck Sequnt ZIC-HILIC guard column (20 x 2.1 mm) using a gradient elution of 0.1 % formic acid in water (solvent A) and ACN (solvent B). The gradient elution started at 20 % of solvent A and increased up to 80 % in 17 min. Then this percentage was maintained during 4 min. The flow rate was set at 400 µL min<sup>-1</sup> and the column temperature and sample tray were held at 23°C and 4°C, respectively.

The Ultimate UHPLC system was coupled to a Q-Exactive instrument (Thermo Fisher Scientific, Bremen, Germany) equipped with a heated electrospray (H-ESI II) ionization source. Nitrogen (purity >

99,995 %) was used as sheath gas and auxiliary gas at flow rates of 45 and 10 a.u. (arbitrary units), respectively. The ion transfer tube was set at 320°C, the vaporizer temperature at 350°C and the electrospray voltage was set at 4 kV in positive mode and -3.5 kV in negative mode. A scanning rate of 2 spectrum s<sup>-1</sup> with a mass range of *m/z* 75 – 800 with a mass resolving power of 70 000 Full Width Half Maximum (FWHM) (*m/z* 200) was used.

Full instrument calibration was performed using a MSCAL5 ProteoMassT LTQ/FT-Hybrid ESI Pos/Neg (Sigma-Aldrich). External mass axis calibration without the use of the specific lock masses was employed. The Xcalibur software version 2.2 (Thermo Fisher Scientific) was used to control the LC-MS system.

The identity of metabolites was confirmed by matching retention times against those of pure chemical standards and accurate masses (<5 ppm). Additionally, the metabolite identities were supported by comparing the observed isotopomers to those expected given the isotope tracers used.

### **Western Blot Analysis**

10 µg of total protein extract per sample was separated on a 4-12 % SDS-PAGE gel (Bolt Bis-Tris Plus, Invitrogen) and transferred to a nitrocellulose membrane using BioRad Trans-blot turbo. After blocking with non-fat milk, the membranes were probed with the following antibodies: mouse anti-α-Tubulin (Santa Cruz DM1A), mouse anti-MYC (Santa Cruz B8.4.B), mouse anti-c-MYC (Santa Cruz sc-40), rabbit anti-HK2 (Atlas Antibodies HPA028587), rabbit anti-SCG2 (Atlas Antibodies HPA011893), rabbit anti-COX5B (Atlas Antibodies HPA034517), rabbit anti-NPM1 (Atlas Antibodies HPA011384), rabbit anti-RPL27 (Atlas Antibodies HPA002649), mouse anti-TH (Abcam ab112) and mouse anti-β-Actin (Santa Cruz C4), followed by anti-mouse or anti-rabbit HRP-conjugated secondary antibodies (DAKO). Bands were detected using ECLTM Western Blotting Detection Reagents (GE Healthcare).

### **Transmission electron microscopy**

The pellets containing approximately 2 x 10<sup>6</sup> cells were fixed in 2.5 % glutaraldehyde in 0.1 M phosphate buffer at room temperature for 30 min. The sections were analyzed using a Tecnai 12 Spirit Bio TWIN transmission electron microscope at 100 kV as previously described (Zirath *et al.*, 2013).

### **Extracellular flux assay**

Oxygen consumption rates (OCR) and extracellular acidification rates (ECAR) were measured using an XFe96 Analyzer (Seahorse Bioscience, Agilent Technologies, North Billerica, MA, US) according to the manufacturer's instructions. Cells were plated at 0.8-1 x 10<sup>4</sup> cells/well on 96-well plates (Seahorse cell culture micro plates) in standard cell culture medium. After 72 h culture medium was exchanged for XF assay medium (Seahorse Bioscience, Billerica, MD), pH 7.4, at 37°C in a CO<sub>2</sub>-free incubator for 1 h before the assay. OCR and ECAR values were reported in pmol/min and mpH/min, respectively. The baseline levels were normalized to protein contents measured by DC protein assay (Biorad) in the XF plates after the experiments were terminated.

### **Soft agar assay**

Assay was performed as previously described (Dzieran *et al.*, 2018). The base layer containing 0.6 % SeaPlaque agarose (Cambrex BioScience-Rockland) in 1x growth medium (from 10x DMEM/F12; Sigma) supplemented with 10 % FBS, 1 % Penicillin/Streptomycin, 0.5 % Glutamax, 1 % non-essential amino acids, was added to the wells of a 12-well plate and allowed to solidify. 1 x 10<sup>4</sup> SK-N-BE(2) cells of a single-cell suspension in 0.4 % SeaPlaque agarose/growth medium were seeded on top of the base layer and, after solidification, covered by growth medium. The agarose-cell suspension and the growth medium were supplemented with 50 µM etomoxir or 50 µM teglicar (Sigma Aldrich Co. LCC) or with vehicle (H<sub>2</sub>O). The medium on top of the soft agar layers was changed every third day. After 10 to 14 days, the living cells were stained by adding 200 µl 5 mg/mL 3-(4,5-Dimethyl-2-thiazolyl)-2,5-diphenyl-2H-tetrazolium bromide (MTT; Sigma Aldrich co. LCC) to the medium and pictures were taken using the ChemiDoc XRS+ System (Bio-Rad Laboratories Inc.). The size and number of colonies were quantified with the OpenCFU software (Geissmann, 2013).

## Immunohistochemistry analysis of tumor sections

For immunohistochemistry (IHC) on SK-N-BE(2) and SK-N-AS xenograft tumors, transverse sections (5  $\mu\text{m}$  thick) from paraffin-embedded tissue were stained with the EnVision GI2 Doublestain System (Dako) according to the manufacturer's instructions. Briefly, paraffin was removed and samples were re-hydrated by consecutive xylol-alcohol gradients. Sample blocking was followed by overnight incubation at +4°C with the following primary antibodies diluted in blocking solution: rabbit anti-Ki67 (1:250, Abcam ab16667), mouse anti-MYCN (1:200, Santa Cruz sc-56729), rabbit anti c-MYC (1:250, Santa Cruz sc-789) or rabbit anti-HIF1 $\alpha$  (1:250, Novus NB100-479). Samples were incubated with secondary antibody for 20 min, followed by 3-5 min incubation with DAB working solution. Nuclear staining with hematoxylin was performed for 2 min. Samples were dehydrated by consecutive alcohol-xylol gradients and mounted with Roti-histokitt mounting medium (Roth).

## Determination of cell viability

For WST-1 viability assay, cells were seeded in 96 well plates and treated as indicated. 10  $\mu\text{l}$  of WST-1 (Roche) were added per well and after 1 h incubation, absorbance at 480 nm was measured in a LUMIstar Omega plate reader (BMG Labtech). For cell growth curves and cell viability determined by cell counting, cells were seeded in 24 well plates and after the indicated treatments and incubation times, cells were trypsinized, mixed with Trypan Blue (Sigma) and counted in a hemocytometer chamber under an inverted microscope.

## Oil Red O (ORO) staining of lipids

Staining was performed as described previously (Zirath et al., 2013). Briefly, cells grown on coverslips were fixed in 4 % (w/v) paraformaldehyde before staining with 0.3 % Oil Red O (Sigma) in 60 % (v/v) isopropanol. For visualization, bright-field images were captured using an Axiovert 40 CFL inverted fluorescence microscope (Zeiss) and Axiovision Rel. 4.8 software.

## QUANTIFICATION AND STATISTICAL ANALYSIS

### Gene set enrichment

The protein profile was analyzed using Gene Set Enrichment Analysis (GSEA), (<http://software.broadinstitute.org/gsea/index.jsp>). Differently expressed proteins (see above) were compared to each of the terms in Gene Ontology. Neuroblastoma patient dataset (Kocak et al., 2013) was analyzed using the R2: Genomics Analysis and Visualization Platform (<http://r2.amc.nl>).

### Statistical analysis

In the proteomics data, the mean of the duplicate values for controls were used to calculate ratios to doxycycline treated samples. Value replicates were filtered based on the ratios between the biological duplicates, by removing proteins outside of 2.17 SD. Proteins were considered to have changed levels compared to control if both of the replicates were > 2.17 standard deviations (97 % confidence, cutoffs 1.4- and 0.7-fold). Metabolic measurements and cell viability assays were analyzed by Student's t-test. Results of the *in vivo* experiment were analyzed using a two-way ANOVA followed by Sidak's multiple comparison tests. All data is presented as mean  $\pm$  standard deviation (SD) with \*, \*\*, \*\*\*, \*\*\*\* indicating  $p < 0.05$ ,  $p < 0.01$ ,  $p < 0.001$  and  $p < 0.0001$ , respectively.

### Gene Expression Analysis

The expression patterns of the differentially expressed proteins in BE (2)sh *MYCN* ON versus BE(2) sh *MYCN* OFF cells were compared to mRNA expression data using a publicly available clinical neuroblastoma data set (Kocak et al., 2013) (GSE45547; NCBI Gene Expression Omnibus), conformed by 649 patients. Data set had complete clinical patient data, including *MYCN*-amplification status, with the exception of 37 samples. In an exploratory data clustering analysis, these 37 samples also showed a clear outlier expression pattern and they were subsequently excluded from further analyses. Normalized data was downloaded from respective data repositories and array probes were matched to gene symbols. Gene expression for multiple probes mapping to the same gene symbol was merged based on average expression on a per sample basis, followed by  $\log_2$  transformation and gene-wise

mean centering. Data was clustered based on Pearson correlation and Ward's method. MYC pathway activity scores were calculated as previously described (Fredlund *et al.*, 2008), with the minor modification that scores were scaled from 0 to 10 in order to enable a fair visual comparison between tumor samples.

### Analysis of patient data

For survival and correlation analyses, two neuroblastoma patient data sets with RNA sequencing expression data from 649 (Kocak *et al.*, 2013) or 88 (Molenaar *et al.*, 2012) patients were used. Clinical and expression data of the genes of interest were extracted from the R2platform (<https://hgserver1.amc.nl/>) and analyzed using Excel and GraphPad Prism softwares.

### DATA AND SOFTWARE AVAILABILITY

The accession number for the proteomics data reported in this paper is ProteomeXchange: PXD015755.

### SUPPLEMENTAL REFERENCES

Dzieran, J., Rodriguez Garcia, A., Westermark, U. K., Henley, A. B., Eyre Sanchez, E., Trager, C., Johansson, H. J., Lehtio, J. & Arsenian-Henriksson, M. 2018. *MYCN*-amplified neuroblastoma maintains an aggressive and undifferentiated phenotype by deregulation of estrogen and NGF signaling. *Proc Natl Acad Sci U S A*, 115, E1229-E1238.

Geissmann, Q. 2013. OpenCFU, a new free and open-source software to count cell colonies and other circular objects. *PLoS One*, 8, e54072.

Henriksen, J. R., Haug, B. H., Buechner, J., Tomte, E., Lokke, C., Flaegstad, T. & Einvik, C. 2011. Conditional expression of retrovirally delivered anti-*MYCN* shRNA as an in vitro model system to study neuronal differentiation in *MYCN*-amplified neuroblastoma. *BMC Dev Biol*, 11, 1.

Kocak, H., Ackermann, S., Hero, B., Kahlert, Y., Oberthuer, A., Juraeva, D., Roels, F., Theissen, J., Westermann, F., Deubzer, H., Ehemann, V., Brors, B., Odenthal, M., Berthold, F. & Fischer, M. 2013. Hox-C9 activates the intrinsic pathway of apoptosis and is associated with spontaneous regression in neuroblastoma. *Cell Death Dis*, 4, e586.

Molenaar, J. J., Koster, J., Zwijnenburg, D. A., Van Sluis, P., Valentijn, L. J., Van Der Ploeg, I., Hamdi, M., Van Nes, J., Westerman, B. A., Van Arkel, J., Ebus, M. E., Haneveld, F., Lakeman, A., Schild, L., Molenaar, P., Stroeken, P., Van Noesel, M. M., Ora, I., Santo, E. E., Caron, H. N., Westerhout, E. M. & Versteeg, R. 2012. Sequencing of neuroblastoma identifies chromothripsis and defects in neuritogenesis genes. *Nature*, 483, 589-93.

Oberthuer, A., Berthold, F., Warnat, P., Hero, B., Kahlert, Y., Spitz, R., Ernestus, K., Konig, R., Haas, S., Eils, R., Schwab, M., Brors, B., Westermann, F. & Fischer, M. 2006. Customized oligonucleotide microarray gene expression-based classification of neuroblastoma patients outperforms current clinical risk stratification. *J Clin Oncol*, 24, 5070-8.

Ribeiro, D., Klarqvist, M. D. R., Westermark, U. K., Oliynyk, G., Dzieran, J., Kock, A., Savatier Banares, C., Hertwig, F., Johnsen, J. I., Fischer, M., Kogner, P., Loven, J. & Arsenian Henriksson, M. 2016. Regulation of Nuclear Hormone Receptors by *MYCN*-Driven miRNAs Impacts Neural Differentiation and Survival in Neuroblastoma Patients. *Cell Rep*, 16, 979-993.

Thiele, C. 1998. Neuroblastoma Cell Lines. In: MASTERS, J. (ed.) *Human Cell Culture*. Lancaster, UK. Kluwer Academic Publishers.

Zirath, H., Frenzel, A., Oliynyk, G., Segerstrom, L., Westermark, U. K., Larsson, K., Munksgaard Persson, M., Hultenby, K., Lehtio, J., Einvik, C., Pahlman, S., Kogner, P., Jakobsson, P. J. & Henriksson, M. A. 2013. MYC inhibition induces metabolic changes leading to accumulation of lipid droplets in tumor cells. *Proc Natl Acad Sci U S A*, 110, 10258-63.